ARRAY SIGNAL PROCESSING FOR SYNTHETIC APERTURE RADAR (SAR)

THESIS

BY

QIFENG LIU

DECEMBER 2018

UNIVERSITY OF SHEFFIELD

Array Signal Processing for Synthetic Aperture Radar(SAR)

by

Qifeng Liu

B.Eng

A master thesis submitted in partial fulfilment

of the requirements for the award of

Master of Philosophy

Supervisors:

Dr. Wei Liu

and

Dr. Xiaoli Chu

December 2018

At this moment, I would like to express my sincere gratitude to my supervisor, Dr. Wei Liu, for the support and help of my study and related research.

Furthermore, I wish to present my special thanks to my parents for their love, support and encouragement.

Abstract

Synthetic aperture radar (SAR) is a kind of imaging radar that can produce high resolution images of targets and terrain on the ground. At present, most of SAR processing algorithms are based on matched filtering. This method is easy to implement and can produce stable results. However, It also has some limitations. This approach must obey the Nyquist sampling theorem and the resolution depends on bandwidth of pulses. This means that the matched filter approach must be based on a large amount of raw data but the performance is limited. With the development of radar imaging, it is difficult for the matched filtering approach to meet the requirement of high resolution SAR iamges.

In this thesis, a new processing method based on the least squares (LS) beamforming is utilized in the processing of SAR raw data. The model of SAR simulates an virtual linear array. The processing of SAR data can also be seen as a process of beamforming. The 1-D azimuth direction echo data is processed using the beamforming method. Simulation results based on the least squares design method are compared with the matched filtering method and the conventional beamforming method with different windows.

Contents

List of Figures

List of Abbreviations

SAR   Synthetic Aperture Radar

ULA   Uniform Linear Array

DoA   Direction of Arrival

SNR   Signal-to-Noise Ratio

TBP   Time-Bandwidth Product

LFM   Linear Frequency Modulated

NFLM   Non-Linear Frequency Modulated

RCM   Range Cell Migration

RCMC   Range Cell Migration Correction

SRC   Secondary Range Compression

ECS   Extended Chirp Scaling

NCS   Non-linear Chirp Scaling

FS   Frequency Scaling

CopSAR   Co-prime Array SAR

PRF   Pulse Repetition Frequency

CS	Compressed Sensing
NP-hardness	Non-deterministic Polynomial-time Hardness
BP	Basis Pursuit
MP	Matching Pursuit
OMP	Orthogonal Matching Pursuit
FFT	Fast Fourier Transform
IFFT	Inverse Fast Fourier Transform
PSLR	Peak Side Lobe Ratio
IRW	Impulse Response Width
LS	Least Squares

Chapter 1

Introduction

1.1   Research Background

In the past 30 years, synthetic aperture radar (SAR) has been widely
applied in a multitude of application fields, such as the geoscience re-
search, the climate change research, the monitoring of Earth system
and environment and even planetary exploration [30]. SAR can be
utilized in the area of earthquake disaster monitoring [37] and map-
ping global surface of other planets, such as Venus, which has a thick
atmosphere [41]. SAR can be considered as an active microwave re-
mote sensing instrument. It transmits electromagnetic waves sequen-
tially, collects echoes reflected from ground targets and stores data in
order to process focused images. Compared with optical imaging sys-
tems, SAR can provide high resolution images without consideration
of daylight, cloud coverage and weather conditions. This is particu-
larly significant in some high latitude areas (polar night) and in some
bad weather conditions [11].

Imaging techniques always desire higher resolution so that we can obtain more details and information from images. SAR is an airborne or spaceborne imaging radar which utilizes the moving of platform to synthesize an antenna with a large aperture. This is why it is called synthetic aperture radar. SAR works in a similar way as a phased array and can be considered as a uniform linear array. The only difference with a phased array with many parallel antennas is that SAR uses only one antenna in time-multiplex. With the moving of the antenna platform, the antenna transmits pulses and collects echoes from different ground targets at different geometric positions and creates an virtual uniform linear array (ULA). Because an virtual ULA is created by SAR, the process of imaging can be treated as array signal processing and we can use methods of array signal processing to obtain focused images. This is why we are expecting to use the beamforming method to acquire a focused image in SAR.

Array signal processing can be divided into two main areas: beamforming [52] [23] and direction of arrival (DoA) estimation [6]. Beamforming, which is also called spatial filtering, is a signal processing technique to form a directional beam for signal transmission and reception [52]. This technique can be achieved by combining elements in different sensors or antennas of an array. Compared with temporal filtering, spatial filtering (beamforming) can separate desired signal from interference even if they occupy the same temporal frequency band [52]. A directional beam, which points to the desired signal, is

formed so that we can collect the desired signal and suppress interference signals. In array signal processing, DoA estimation is another key research field to estimate the direction angle of impinging signals by an antenna array. The DoA estimation has two main research aspects: self-adaption array signal processing and spatial spectrum estimation. These two aspects have developed rapidly adn are still being developed [31].

In the past decades, most of processing algorithms of SAR are based on the matched filter method, such as the range-Doppler algorithm [5] [26], the chirp-scaling algorithm [44] and the $\omega - k$ algorithm [3]. These algorithms convolve the raw data with matched filter reference functions in order to compensate for the phase difference and maximize the value of SNR. However, with the increasing requirement of resolution, the limitations and disadvantages of this method become apparent. For instance, the challenge for hardware due to high sampling rate, high computation, and large on-board memories and downlink throughput. Also, the image resolution obtained by the matched filter method is limited because of the width of mainlobe and the sidelobe effect.

1.2   Research Aims and Objectives

Currently, most of SAR processing methods are based on matched filter. However, the methods based on matched filter have many dis-

advantages and limitations. Firstly, matched filter must obey the Nyquist sampling theorem. The sampling frequency must be larger than the signal bandwidth in order to avoid the distortion. The resolution is related to the signal bandwidth. This means that higher resolution requirement will result in a higher sampling frequency. Large amount of raw data will be created for a high resolution requirement image. It will be a large challenge for the entire hardware system and we need more computation time to proceed the raw data. Secondly, the result of matched filter is a sinc-like function. Because of the effect of side lobes, the resolution could be limited. Two close point targets could not be distinguished.

The main objective of the research is to propose a new SAR data processing method based on array signal processing. The key point of this research is to treat the SAR data processing as a problem of array signal processing. SAR created an virtual array in time-multiplex. We can start a new direction of view to see the problem of SAR data processing. Compared with matched filter method, the beamforming method has many advantages. The resolution of image will improve and the side lobes will be mitigated by using beamforming method. The aim of this research is not only to improve the quality of SAR image, but also to reduce the amount of raw data. After utilizing the beamforming methods in SAR processing, we are going to utilize the concept of sparse array to change the ULA of conventional SAR to a sparse array. This method can result in fewer sampling points and

lower amount of raw data.

1.3　Contributions of Thesis

In this thesis, the main contribution is to utilize the least squares beamforming method to preceed the SAR raw data. Compared with the conventional SAR processing methods based on matched filter, the processing method based on least squares beamforming decreases the value of side lobes and improves the qualtity of SAR image. Furthermore, we complete the preparation work to combine the SAR processing and the array signal processing. A new direction view of SAR processing is made so that we can research the utilization of beamforming method based on sparse array in the SAR processing. This is an important research field to reduce the amount of SAR raw data.

1.4　Thesis Outline

In Chapter 1, we explain some essential features of SAR and array signal processing and some processing algorithms based on matched filter will be introduced generally. Then, in Chapter 2, a general literature review about SAR model and basic processing methods is given to discuss the basic concepts of SAR and limitations of existing processing methods. In Chapter 3, the most commonly used algorithm, the range-Doppler algorithm, and the co-prime array SAR (CopSAR)

are introuced with details. Some simulation results of both point and area target are provided with these two approaches. In Chapter 4, the processing method based on the least squares beamforming is utilized in the processing of SAR data. The first part of Chapter 4 discusses the conventional beamforming method for SAR with different types of windows, such as rectangular window, Hamming window, Hanning window, Blackman window and Kaiser window. The second part of this chapter focuses on the least squares beamforming in details and some simulation results of this method are shown to compare with conventional beamforming method. Then, Chapter 5 gives the conclusion of this thesis and some future work in this research field, such as beamforming method based on sparse array for SAR data processing and beamforming method under the framework of compressed sensing for SAR data processing.

Chapter 2

Literature Review of SAR Model and Basic Processing Methods

2.1 Introduction to Synthetic Aperture Radar

2.1.1 Concept of Synthetic Aperture Radar

Synthetic aperture radar (SAR) is a kind of radar imaging technology that is often used to produce two-dimensional (2-D) images of ground targets. Imaging radar is an active illumination system [42]. An antenna, which is mounted on a moving aircraft or spacecraft, transmits electromagnetic wave periodically in a side-looking direction towards the ground. The echo is back-scattered from target on the ground and the amplitudes and phases of echo are collected by the same antenna. The realization of SAR is a marriage of the radar techniques and the signal processing techniques. 2-D images produced by SAR have two dimensions. One dimension is called azimuth (or along track), which is the same as the direction of platform. Another dimension is called range (or cross track) and is perpendicular to the azimuth direction.

In the azimuth direction, high azimuth resolution is obtained by using aperture synthesis. The resolution of a radar system is the ability to distinguish two objects separated by minimum distance. If objects are separated, they will be located in different resolution cell and be distinguishable. If not separated, the image will show a complex combination of the reflected energy from two objects [42]. For the azimuth resolution in SAR, beam width is the key parameter to separate objects. Radar can only distinguish two objects in different beams. If two objects are illuminated by the same beam, they will be indistinguishable and be seen as same object. This means that we must decrease the beam width of radar to increase resolution. The half-power angular beam width (β) of radar is a direct function of radar wavelength (λ) and an inverse function of antenna aperture (D), which is

$$\beta = \frac{\lambda}{D} \tag{2.1}$$

The corresponding azimuth beam width (L) at range R is

$$L = \beta R \tag{2.2}$$

Therefore, the azimuth resolution (ρ_a) is

$$\rho_a = \frac{\lambda}{D} R \tag{2.3}$$

According to Equation (2.3), we can increase D to make the beam width smaller and obtain a better resolution. To obtain high azimuth resolution, a physically large antenna is needed to focus the transmitted and received signals into a sharp beam [27]. While the platform of

SAR moving ahead and antenna transmitting pulse periodically, the SAR system simulates an uniform linear array and synthesizes a large antenna aperture, which is shown in Figure 2.1. At positions A, B, C and D, the antenna transmits and receives coherent signals to the target ship. Due to this coherence of signals, SAR can create a sharp beam and the synthetic aperture length is the distance from A to D in figure.
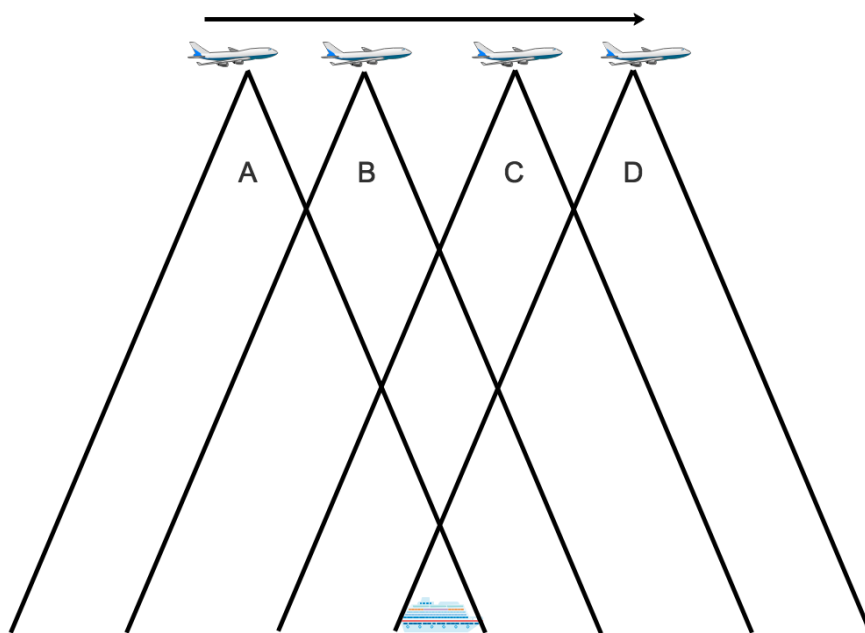
Figure 2.1: Concept of aperture synthesis.

Then, we can calculate the theoretical azimuth resolution of SAR. Firstly, we need to point out that the flying mode of SAR is assumed as the straight flight. The antenna of SAR is fixed on the platform of aircraft or satellite. The antenna moves straightly in a fixed velocity direction vector. All the following signal model, equations and analysis are all based on this assumption. The synthetic aperture length (L_s) is the beam width of physical aperture antenna at range R, which

is

$$L_s = \frac{\lambda}{D} R \tag{2.4}$$

Hence, the azimuth resolution of SAR is

$$\rho_a = \frac{1}{2} \frac{\lambda}{L_s} R = \frac{D}{2} \tag{2.5}$$

where the one-half factor is because SAR uses the same antenna for transmission and reception and radar signals travel through two-way path between the antenna and the target. We can find that the azimuth resolution is only dependent on the physical aperture of antenna of SAR and has no relationship with wavelength and distance from the target. Moreover, this result indicates higher resolution is achievable with smaller rather than larger physical aperture, which is contrary of other kinds of radar. It appears surprising on the first view of this equation. However, we can become clear that a shorter antenna sees a point target on the ground for a longer time. This is because a shorter physical antenna length can produce a larger angular beam width so that we can have a longer illumination time of a point target. This is equivalent to a longer virtual synthetic aperture length and a higher azimuth resolution. However, this does not mean that an infinitesimal antenna will obtain an extremely high azimuth resolution. For example, we could simply build an antenna with length of 1cm to obtain a 5mm resolution of azimuth direction. This is completely impossible. The length of physical antenna length must be large enough so that we can create the proper interference pattern between the dipoles of antenna for the beam spread. An extremely small antenna aperture

will create an abnormal beam pattern and result in an ambiguous image . In fact, the motion between SAR and target has Doppler effect. The resolution is also related with Doppler bandwidth. This will be discussed in the following section about SAR signal properties.

In the range direction, the fundamental idea of getting high resolution is the same as most radars. The range resolution determines the width of range gates or bins [14]. From the radar fundamentals, we can know that the distance between antenna and target is

$$R = \frac{c\Delta t}{2} \qquad (2.6)$$

where c is the speed of light and Δt is the time delay between transmitting pulse and receiving echo.
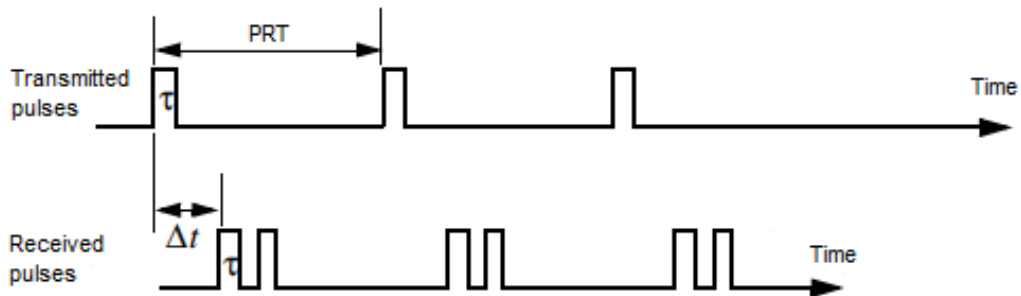

Figure 2.2: Train of transmitted and received pulse.

The train of transmitted and received pulses are shown in Figure 2.2. We can know that two echoes must have time difference so that they can be distinguished by radar. The minimum time difference between two distinguishable objects (two echoes are critically over-

11

lapped) is the time duration of pulse (τ_p). Hence, the range resolution of SAR can be given by

$$\rho_r = \frac{c\tau_p}{2} = \frac{c}{2B} \tag{2.7}$$

where B=$1/\tau_p$ is the bandwidth of pulse transmitted [14]. In order to obtain high range resolution, the pulse transmitted should be narrow, which means small time duration and large bandwidth. However, energy transmitted by a narrow pulse is insufficient and it will be difficult for the radar to collect the echoes. To deal with this problem, the pulse compression technique was developed and utilized in SAR. In general, narrow pulse used in radar always has unit Time-Bandwidth Product (TBP). However, in a pulse compression system, a wide pulse having a time duration T_0 and a bandwidth B, where $T_0 \cdot B$ is much greater than one (unit), is somehow transmitted. Received echoes are processed in such a way that narrow pulses having a time duration $T_p = \frac{1}{B}$ are obtained [43]. The ratio of time duration of wide pulse T_0 to that of narrow pulse T_p is a significant parameter called compression ratio K_p,which is given by

$$K_p = \frac{T_0}{T_p} = T_p \cdot B \tag{2.8}$$

For the pulse compression technique, some kinds of pulses can be used, such as the linear frequency modulated (LFM) signal, the non-linear frequency modulated (NLFM) signal and the phase-coded signal. LFM signal is chosen for pulse compression in SAR. This pulse compression technique maintains both high range resolution of narrow pulses and target detectability of wide pulses [43].

2.1.2 Geometric Model of SAR

The purpose of this part is to describe a general data acquisition geometric model of SAR and to define some geometry-related terms. Figure 2.3 shows a general model of a SAR regarding radar location and beam footprint illuminated on the Earth's surface. The SAR image formation create an image in slant range (not ground range) and azimuth coordinates.
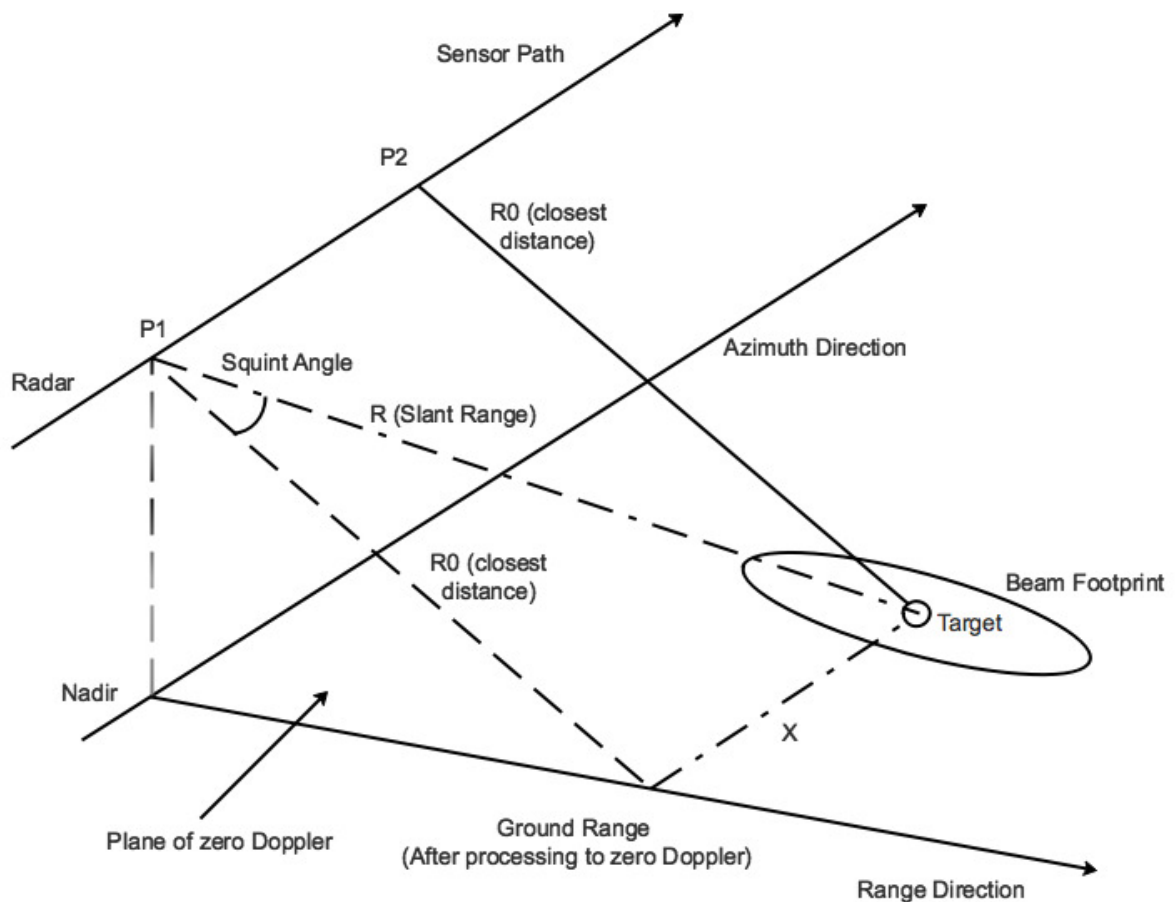
Figure 2.3: SAR data acquisition geometric model.

In Figure 2.3, The target is a hypothetical point on the Earth's surface. The SAR systems actually images an area, but this point target is used more easily to develop SAR theories [50]. The radar beam is viewed as a cone and the footprint is the intersection of the cone with ground. The footprint of a single beam is an ellipse, but the whole footprint area will be a stripe on the ground due to the platform moving. The nadir is the point on the Earth's surface, which is directly below the antenna. Hence, the normal to the Earth's surface at the nadir passes through antenna. The zero Doppler plane is a plane that is perpendicular to the platform velocity vector direction and the azimuth direction. The intersection of the zero Doppler plane with ground is called the *zero Doppler line*. The squint angle θ_{sq} in the figure is an angle between the antenna beam pointing direction vector and the zero Doppler plane. If the squint angle is zero, the beam direction vector is perpendicular to the platform velocity vector and the SAR is side-looking. The parameter R is the slant range between antenna and target. During the moving of platform, the distance R will decrease gradually until platform moves to the closest point with target, where R becomes R_0, and then it will increase again. Hence, R_0 is called *range of closet approach* when the slant range is minimum (when the *zero Doppler line* crosses the target). The line of R_0 is perpendicular to the platform velocity vector direction.

2.1.3 SAR Signal Properties

In SAR, linear frequency modulated(LFM) signal, which is also called chirp signal, is used for pulse compression. The properties of LFM signal will be introduced firstly. LFM signal is a kind of modulated signals in which the frequency increases or decreases with time. [39]. The relationship of time and frequency of the LFM signal is a linear function. The mathematical equation can be expressed as

$$s(t) = rect\left(\frac{t}{T_0}\right) exp\left\{j2\pi f_c t + j\pi K t^2\right\} \tag{2.9}$$

where t is the time variable in seconds, T_0 is time duration of the LFM signal, f_c is carrier frequency and K is the linear FM rate in Hz/s. The instantaneous frequency is the derivative of phase and can be expressed as

$$f = \frac{1}{2\pi}\frac{d\phi(t)}{dt} = \frac{1}{2\pi}\frac{d(2\pi f_c t + \pi K t^2)}{dt} = f_c + Kt \tag{2.10}$$

This means that the frequency is a linear function of time t with the slope K. The waveform of LFM signal is shown in Figure 2.4.

In SAR, both signals in the range and azimuth directions can be considered as LFM signal. Matched filtering approach is used for LFM signal pulse compression. Matched filter is designed to do the correlation process and cancel the quadratic phase term of LFM signal and the equation is given by

$$h(t) = s^*(-t) = rect\left(\frac{t}{T_0}\right) exp\left\{j2\pi f_c t - j\pi K t^2\right\} \tag{2.11}$$
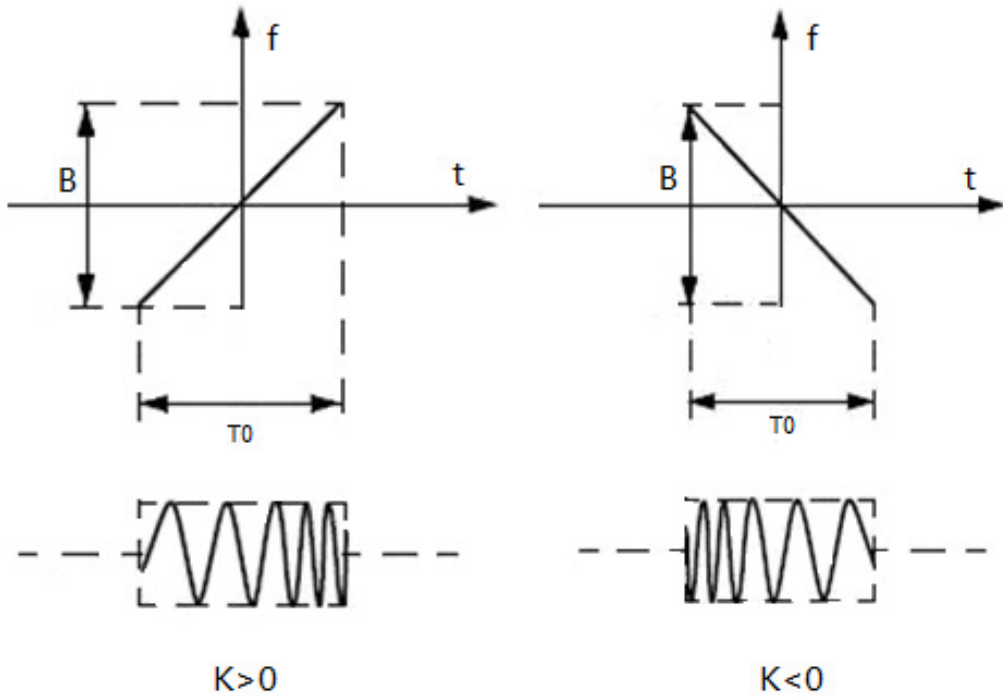
Figure 2.4: LFM signal waveform.

After convolution with matched filter and removing carrier frequency, the output can be given by

$$s_0(t) = s(t) * h(t) = T_0 rect\left(\frac{t}{T_0}\right) sinc(\pi B t) \qquad (2.12)$$

where the $*$ is the mark of convolution calculation. The waveform of output signal is shown in Figure 2.5. After pulse compression, signal changes to a narrow pulse with unit TBP. Hence, the pulse width of this output signal $T_p = \frac{1}{B}$ and the compression ratio $K_p = \frac{T_0}{T_p} = T_0 B$.

It is clear that the final output after pulse compression should be a sinc function. Hence, the output of a point target should be two orthogonal sinc functions in SAR image space.

In the range direction of SAR, the equation of transmitted LFM
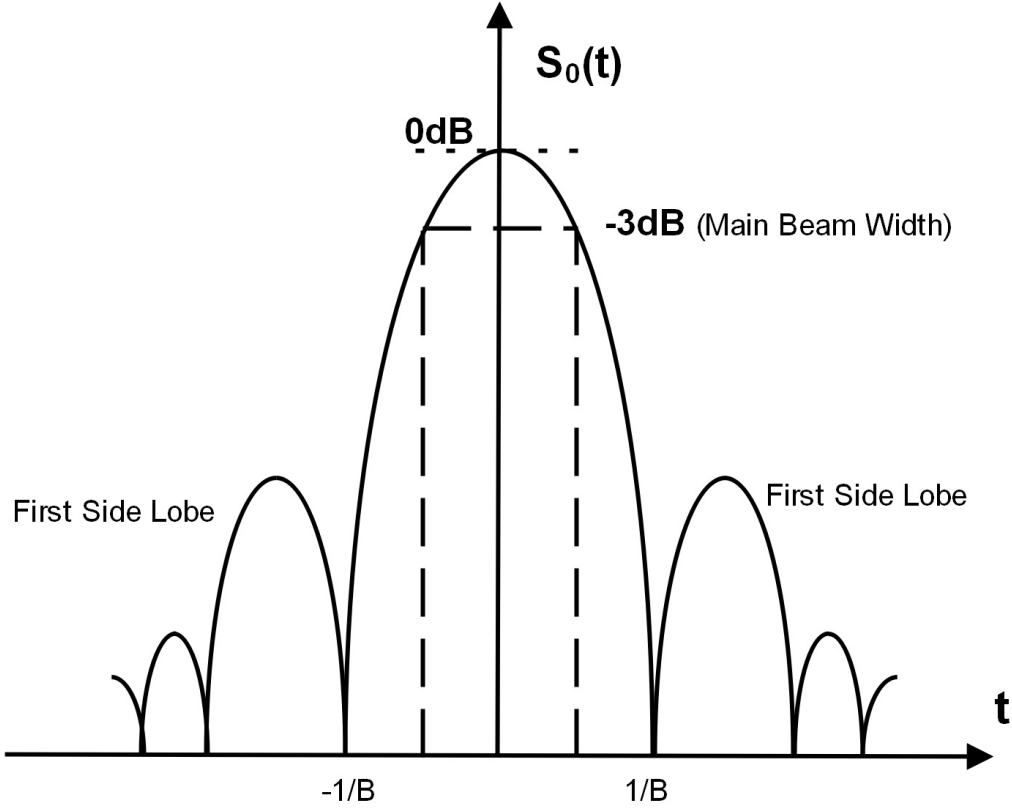
Figure 2.5: Output signal after pulse compression.

signal can be given by

$$s_{pul}(\tau) = w_r(\tau)cos\left\{2\pi f_c \tau + \pi K \tau^2\right\} \qquad (2.13)$$

where $w_r(\tau) = rect\left(\frac{\tau}{T_0}\right)$, which is assumed as a rectangular pulse envelope, and τ is the range time (fast time). This LFM signal is transmitted to ground by antenna and reflected by objects on the ground.

Next, we will discuss how the echoes are acquired across a range swath. The radar beam has an elevation beam width in the elevation plane and it is shown in Figure 2.6. The reflected energy at any illumination instant is a convolution of transmitted pulse and the ground

reflectivity g_r [9], which can be expressed

$$s_r(\tau) = g_r(\tau) * s_{pul}(\tau) \tag{2.14}$$

where the mark of $*$ means the convolution calculation. Consider a point target at a range distance R_a away from antenna, with the magnitude A_0, which is back-scattered reflection coefficient σ_0. Hence, the ground reflectivity is $g_r(\tau) = A_0 \delta(\tau - 2R_a/c)$, where the $2R_a/c$ is the time delay of the signal for reflector. the echo $s_{pul}(\tau)$ from the point target is

$$s_r(\tau) = A_0 s_{pul}(\tau - 2R_a/c)$$
$$= A_0 w_r(\tau - 2R_a/c)\cos\left\{2\pi f_c(\tau - 2R_a/c) + \pi K(\tau - 2R_a/c)^2 + \psi\right\} \tag{2.15}$$

Figure 2.6: Elevation beam width in elevation plane.

18

In the azimuth direction, we need to consider the Doppler effect to analyze the SAR signal. The geometry side-looking model SAR is shown in Figure 2.7. The slant 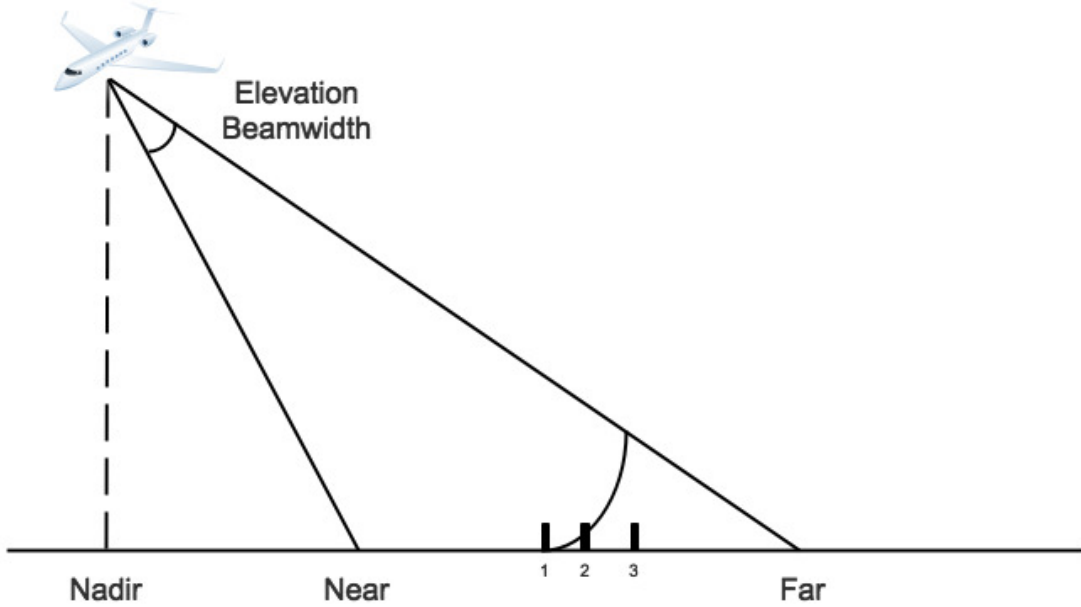distance between antenna and point target decreases firstly until the closest slant distance R_0, and then increases again. Assume the coordinate of point target A is $(0, Y_0, 0)$, v_a is the velocity of platform and η is the azimuth time (slow time). Y_0 is the ground range which has a relationship with platform height H and the closest slant distance R_0, i.e. $Y_0 = \sqrt{R_0^2 - H^2}$. The instantaneous slant distance $R(\eta)$ is given by [12]

$$R(\eta) = \sqrt{R_0^2 + x^2} = \sqrt{R_0^2 + v_a \eta^2} \qquad (2.16)$$

In the general case, the closest slant distance R_0 is much larger than the moving distance of platform $v_a \eta$. Hence, using Taylor series expansion, the instantaneous slant distance can be approximated as

$$R(\eta) = \sqrt{R_0^2 + v_a \eta^2} \approx R_0 + \frac{v_a \eta^2}{2R_0} \qquad (2.17)$$

Compared with transmitted pulses, the echoes have time delay and the Doppler frequency shift [12]. Because of the relative motion between platform and point target, the instantaneous phase of the azimuth direction signal is

$$\phi(\eta) = -2\pi \frac{2R(\eta)}{\lambda} = -2\pi \frac{v_a^2}{\lambda R_0} \eta^2 + Constant \qquad (2.18)$$

where the minus sign is because the echoes lag behind the transmitted pulses. The instantaneous frequency of echoes in the azimuth direction is the derivative of Equation (2.18) and can be expressed as

$$f(\eta) = \frac{1}{2\pi} \frac{d\phi(\eta)}{d\eta} = -\frac{2v_a^2}{\lambda R_0} \eta \qquad (2.19)$$

It is apparent that the instantaneous frequency is a function with time, which can be considered as a LFM signal. Therefore we can also use pulse compression to process azimuth echoes. The relative motion between antenna and point target results in the phase shift with time and linear variation of instantaneous frequency, which is known as Doppler shift. More generally, the instantaneous frequency is

$$f(\eta) = f_{dc} + K_a\eta = -\frac{2v_a^2}{\lambda R_0}\eta + const \qquad (2.20)$$

where f_{dc} defines the Doppler centroid and K_a is linear FM rate of azimuth signal. If the working model is side-looking (squint angle is zero), the Doppler centroid is zero. If the working model is not side-looking, the Doppler centroid is a constant.
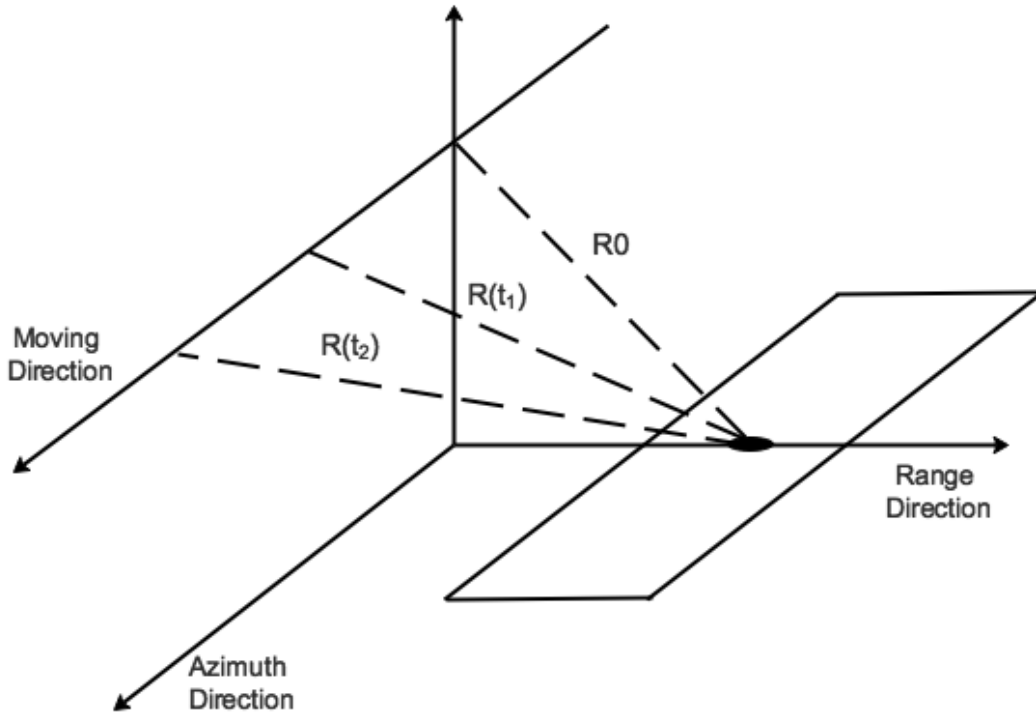

Figure 2.7: Side-looking model SAR geometry.

After analyzing both the range signal and the azimuth signal, the two-dimensional signal, which is demodulated to baseband, can be expressed as

$$s_0(\tau, \eta) = A_0 w_r(\tau - 2\frac{R(\eta)}{c}) w_a(\eta - \eta_c) exp\left\{-j4\pi f_c R(\eta)/c + j\pi K(\tau - 2\frac{R(\eta)}{c})^2\right\}$$

$$(2.21)$$

where the τ is the time in the range direction and the η is the time in the azimuth direction. This equation represents raw data of the point target collected by antenna [12]. Many imaging algorithms, such as the range-Doppler algorithm [5] [26], the chirp-scaling algorithm [44] and the $\omega - k$ algorithm [3], have been developed to process raw data and obtain focused images. These algorithms are all based on matched filter to acquire the focused image [50] [12].

According to Equation (2.21), it is obvious that the raw data is two-dimensional. The data of range direction can be processed by pulse compression technique, which is implemented by the matched filter method. The data of the azimuth direction can be seen as the data of an virtual array, which means that the data can be processed by the beamforming method. For a beamforming based processing method, the point target expression can be represented by

$$s_0(\eta) = A_0 w_a(\eta - \eta_c) exp\left\{-j4\pi f_c R(\eta)/c\right\} \qquad (2.22)$$

where the exponential phase is caused by relative motion between point target and radar. The purpose of processing is to remove the exponential phase of SAR data to acquire clear images. Because the

raw data in the azimuth direction can be seen as the data collected by an virtual uniform linear array, we can utilize the beamforming method to process data.

2.2 Review of Matched Filter Based Processing Methods

The Processing of SAR raw data requires a correlation of the collected SAR raw data with the reference functions of the azimuth and the range directions. Different reference matched filters are utilized in the azimuth and range directions separately. The 2-D correlator in the time domain can complete the correlation steps, but is computationally inefficient [3]. For taking the advantages of fast processing speed in the frequency domain, several processing algorithms have been developed in the decades with different correlation kernels.

The first digital processing algorithm is called range-Doppler algorithm, which is developed by J. Bennett and I. Cumming [12] [5]. For more than four decades the range-Doppler algorithm has been the basis of the most accurate and widely used SAR processing algorithm [26]. It has three main steps, range compression, range cell migration correction (RCMC) and azimuth compression. Several modifications of this algorithm are proposed to improve its performance. The most important modification is the secondary range compression (SRC), which is used to solve the problem of large squint angle [29].

The range-Doppler algorithm performs the range compression in the range frequency domain, the RCMC in the azimuth frequency and the range time domain and the azimuth compression in the azimuth frequency domain. This algorithm will be introduced with details and simulation results will be shown in Chapter 3.

In the range-Doppler algorithm, the step of RCMC uses the interpolation operation, which requires both computation time and accuracy of processed image. The chirp scaling algorithm is proposed by R. Raney to avoid interpolations and perform the RCMC accurately [26] [44]. This algorithm modulates the frequency of chirp signal and makes the scaling of chirp signal. This is why this algorithm is called chirp scaling algorithm. Phase multiplications using matched filter are used to replace the interpolations that need long computation time in the range-Doppler algorithm. This algorithm requires only complex multiplications and Fourier transform. Compared with the range-Doppler algorithm, chirp-scaling is usually used in large swath and large squint angle scenario. In order to acquire higher accuracy, many modifications based on the chirp-scaling algorithm are proposed, such as the extended chirp scaling (ECS) algorithm [35], the nonlinear chirp scaling (NCS) algorithm [15] and the frequency scaling (FS) algorithm [34].

After the chirp-scaling algorithm, a new class of algorithms were then proposed and implemented in order to reduce the approximation

error further. They are refereed to as the $\omega - k$ algorithm, which processes data in the two-dimensional frequency domain [3] [36] [8]. This algorithm is based on Stolt interpolation and can match with the SAR echo signal perfectly. Hence, it has high processing accuracy. In the chirp-scaling algorithm, it uses approximations for SAR data processing, which could be invalid in some scenarios. In order to slove this problem, the $\omega - k$ algorithm was formulated in terms of wave equation. The problem of original the $\omega - k$ algorithm is motion compensation is not accurate. In order to solve this problem and make the algorithm more practical, an extend the $\omega - k$ algorithm was proposed [45] [46].

These algorithms are three main SAR processing algorithms based on matched filter in the frequency domain. They all use some transformations and approximations to do the matched filtering in the frequency domain. In different applications, they have different modifications in order to improve the image quality. In addition to those frequency domain processing algorithms, there is another branch of SAR data processing, which is the time domain processing algorithms. The most typical algorithm is the back-projection algorithm [12]. In theory, this algorithm can match with SAR echo signal perfectly without any transformation or approximation. This is the most accurate algorithm based on matched filter. However, extremely large computation time for correlation between the SAR echo signal and reference function matched filter is required. Hence, it is seldom used in prac-

tice and only used for scenarios with a small observing area.

Based on the theoretical framework of matched filter, many modifications of different algorithms are still being proposed to improve the image quality. However, because of some features of matched filter, the improvement of these algorithms could be limited and these are the limitations of matched filter based algorithms.

2.3 Limitations and Existing Solutions of Matched Filter Based Processing Methods

2.3.1 Limitations of Matched Filter Based Processing Methods

In general, most of processing algorithms are based on the same theoretical framework, which is the matched filter. Matched filter is a linear process and easy for implementation. However, it also has several obvious disadvantages and limitations.

Firstly, The algorithms based on matched filter must obey the Nyquist sampling theorem. In order to avoid distortion of waveform, the sampling frequency must be larger than signal bandwidth. This means the amount of raw data will be much large for a high resolution requirement image. Moreover, because the resolution is related to the signal bandwidth, higher resolution requirement need a higher

bandwidth. This will result in a higher sampling frequency and it will be a big challenge for the analogue-to-digital converter and the entire hardware system [28].

Secondly, the result of matched filter is a sinc-like function. This means that the image of an ideal point target will be a two-dimensional impluse response with a certain width and the effect of side lobes [12]. Because of this reason, the resolution improvement of matched filter based algorithm could be limited. For two close point targets, they will be distinguishable and ambiguities without any detailed information. Also, because the main lobes and side lobes of different point targets can affect each other, the image processed by matched filter will have coherent speckle noise and affect the resolution of image.

2.3.2   Existing Solutions for Limitations of Matched Filter

According to the last section, it is clear that what are the problems of the matched filter based processing method. The most significant problem is the high sampling frequency, which results in large amount of sampling points and large amount of stored and processed data, for high resolution requirement imaging. To reduce the amount of sampling points (amount of data stored and processed), G. Martino proposed a co-prime synthetic aperture radar (CopSAR) [16] [33]. Compared with the uniform linear array of conventional SAR, CopSAR uses one kind of sparse array, which is called co-prime array. Co-prime

array is a combination of two uniform linear arrays with different inter-element spacing. The two values of different inter-element spacing of two arrays are two co-prime number times a constant distance d. This means that they have no common factors except unity. As a result, the elements of two arrays do not overlap. In the proposed algorithm in this paper, a new SAR modality is proposed to transmit two interlaced sequences of pulses to build the co-prime array. In SAR, pulse repetition frequency (PRF) means the inter-element spacing of arrays. The PRF of conventional SAR corresponds to the aforementioned distance d. This means that the PRFs of two sub-arrays of the co-prime array is smaller than PRF of the conventional SAR. It means that the spacing of inter-element is larger than d. The PRFs of two sub-arrays are smaller than Nyquist frequency. The data received by two sub-arrays are processed by matched filter algorithm separately. This means that the processed images will be severely aliased with many ghost replica targets. Different PRFs will cause different locations of ghost targets in two processed images.

The proposed algorithm in this paper can only be used when the observation area consisting of bright targets on a dark background (such as the scene of ships on the ocean surface), which is similar to the scenario of some point targets. The impulse response of true target will be on the two aliased images at the same locations on the two images. In one of the two aliased images, it shows the replica of target. However, in the other image, it only show the sea background in

27

the same location. By comparing the two images, selecting the smallest modulus of two images to remove the replica targets. Conversely, wherever the true target is present, the two images will have similar high moduli. Even a smaller one is selected, the final image still has the correct pixel.

In [33], the authors proposed three modes, which are basic implementation, missing-pulse implementation and dual-frequency implementation. The proposed approach can reduce the amount of data and increase the range swath at the same time without any resolution loss. It is based on adaption of the co-prime array concept to the case of SAR systems. In [17] and [18], G. Martino proposed an improved CopSAR, which is called Orthogonal Co-prime SAR (OrthoCopSAR). This is an improvement of the basic implementation mode of CopSAR, which is based on transmission of (quasi) orthogonal waveforms. This approach can reduce the amount of data and increase the range swath without any ghost target.

These approaches have been tested by using simulated and real data of SAR. It is suitable for ocean and maritime scenario. It is based on co-prime array concept and matched filter. In the other word, these approaches still use matched filter to process data without improving the sampling method. The most significant problem with these approaches is that it is only suitable for scenario of some point targets (ocean ship detection). By using the approach of selecting the lowest

modulus of two images, the true point target will be removed if it is in the location of replica target of another point target. This means that this approach cannot be used for an image with many high reflected coefficient targets, such as mapping of the ground. Also, these proposed approaches only use the concept of co-prime array. They do not utilize any array signal processing method such as beamforming or direction of arrival (DoA) estimation in their processing and still use conventional matched filter algorithms to process data. These approaches can be used as a reference to propose new SAR processing method based on array signal processing of co-prime or other kind of sparse arrays.

Another approach to reduce amount of data and mitigate the effect of sidelobes is using the theory of compressed sensing. In recently years, compressed sensing (CS) has been applied in the field of SAR imaging. The reason why SAR cannot reduce the amount of data using matched filter is because we must obey the Nyquist sampling theorem to avoid aliasing. Under the framework of compressed sensing, it is possible to reconstruct the sparse or compressible signals with fewer amount of data [10] [4] [19]. Compressed sensing SAR uses priori information of SAR, which is the sparsity of SAR data. In [53], the authors proposed sparse signal representation from complete dictionaries based on the CS theory. In [6], a technique for the compression of raw data is proposed based on the use of continuous wavelet transform in order to obtain a sparse representation of the complex

SAR image. In [22], the authors proposed a method to reduce the amount of stored SAR data based on compressed sensing. In [21], based on the approximated observation, a new SAR fast compressed sensing method is proposed.

Under the framework of compressed sensing, the two main problems are choosing the measurement matrix to represent the SAR signal and choosing different reconstruction algorithms to rebuild signal in different scenarios. The reconstruction in the CS framework is to solve an l_0 norm minimization problem. In [20], Donoho points out that this is a NP-hardness (Non-deterministic Polynomial-time Hardness) problem and difficult to solve. The most common approach is to use l_1 norm minimization to replace the original problem. In [9], the authors proved that they could reach the same solution. The first method to solve l_1 norm minimization problem is using basis pursuit (BP). This method can solve the problem based on convex optimization. Another method is called matching pursuit (MP), which is a kind of greedy algorithms.

In [7], B. Han proposed a compressed sensing SAR imaging based on co-prime arrays sampling. Co-prime is widely used in the field of DoA estimation and can achieve a higher number of degrees of freedom. High degrees of freedom means more signal information. This means this co-prime array sampling structure can obtain enough information of the signal by non-uniform low speed sampling. The mea-

surement matrix is obtained by the transformation of sampling array. In this proposed algorithm, the orthogonal matching pursuit (OMP) greedy algorithm, which is an enhancement of the MP method, is used to reconstruct the signal. Some simulations of several point targets and small area target are shown.

Compressed sensing theory uses the sparsity of SAR signal. Sparsity means only a small portion of the observing area has targets, such as several point targets or small area target. This means that proposed approaches based on compressed sensing cannot process SAR data of ground mapping, where targets are on the entire observing area. For a scenario that is not sparse, we can use sparse representation to represent SAR data, which means making the SAR data sparse in the other domain. However, the sparse representation for SAR data is difficult because echo signals reflected by different targets have random phase. New approach is still being proposed to solve this problem.

Chapter 3

SAR Raw Data Processing Approaches

The raw data received from the radar system must be processed in order to acquire focused image. Currently, most of algorithms to process data are based on matched filter. In the time or frequency domain, the matched filter is used to compensate the phase difference of signals received by different sensors (sampling points) of the virtual array. In the following section, one of the most commonly used algorithm, which is called the range-Doppler algorithm, is introduced and simulation results of point target and area target are shown. Then, a introduction of co-prime SAR (CopSAR) is shown with details, which introduces the concept of co-prime array and the CopSAR. Also, some simulation results are presented as follows.

3.1 The range-Doppler Algorithm

3.1.1 Introduction to the Algorithm

The range-Doppler algorithm processes the raw data calculated from Equation (2.21), which have been first demodulated to baseband, to produce the focused SAR image. This algorithm separately performs pulse compression via the matched filtering in the Fourier transformed range and azimuth domains [26]. For processing time efficiency, the Fourier transforms are processed using fast Fourier transforms (FFTs). Due to the slant range always changes during the motion of platform, this change results in the range cell migration and the coupling between the range and azimuth directions. The range cell migration correction (RCMC) is performed in the range time and the azimuth frequency domain, which is called the range-Doppler domain. This is why this algorithm is called the range-Doppler algorithm. Performing the RCMC in this range-Doppler domain is the defining feature of the algorithm when compared with other processing algorithms. In Figure 3.1, a block diagram of the range-Doppler algorithm is shown. There are three main steps of the range-Doppler algorithm, which are the range compression, the RCMC and the azimuth compression [12].
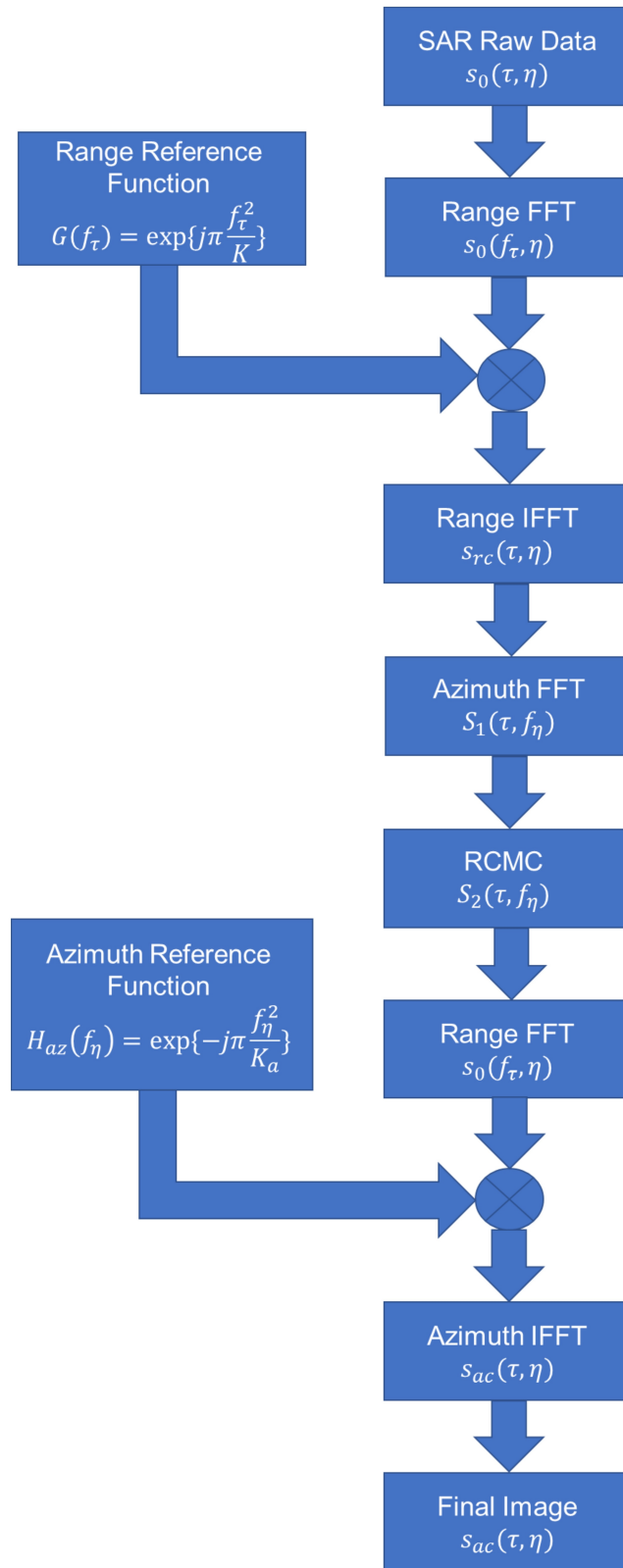
Figure 3.1: Block diagram of range-Doppler algorithm.

In Section 2.1.3, the matched filtering in the time domain is completed by using the convolution operations. As we known, the convolution operations are the same as the multiplication operations in the frequency domain. We only need to transform the raw data and the matched filter reference functions into the frequency domain. Compared with the convolution operations in the time domain, the multiplication operation is much easier in computation so that the processing time will decrease dramatically. Hence, all steps of this algorithm are all based on the frequency domain.

Firstly, the two-dimensional signal $s_0(\tau, \eta)$ is analyzed as a series range time signals for each azimuth bin. The equation of this signal is shown in Equation (2.21). The variable τ is the time of the range direction (fast time) and the η is the time of the azimuth direction (slow time). The signals of the range direction are transformed into the frequency domain via FFT, which can be expressed as $S_0(f_\tau, \eta)$. The range compression is performed in the range frequency domain. The matched filter in the range frequency domain is defined as $G(f_\tau) = exp\left\{j\pi\frac{f_\tau^2}{K}\right\}$ and is multiplied with signals $S_0(f_\tau, \eta)$. The matched filter is used to remove quadratic phase of signal and compress chirp signal into a sinc function in the range direction. After performing IFFT and transforming back to the range and azimuth time domain, the signals can be represented as

$$
\begin{aligned}
s_{rc}(\tau, \eta) &= IFFT_\tau\{S_0(f_\tau, \eta)G(f_\tau)\} \\
&= A_0 p_\tau[\tau - 2R(\eta)/c]w_a(\eta - \eta_c)exp\{-j4\pi f_c R(\eta)/c\}
\end{aligned}
\tag{3.1}
$$

where the compressed pulse envelope $p_r(\tau)$ is the IFFT of the window $W_r(f_\tau)$. For a rectangular window, $p_r(\tau)$ is a sinc function. For a tapered window, it will be a sinc-like function with lower side lobes.
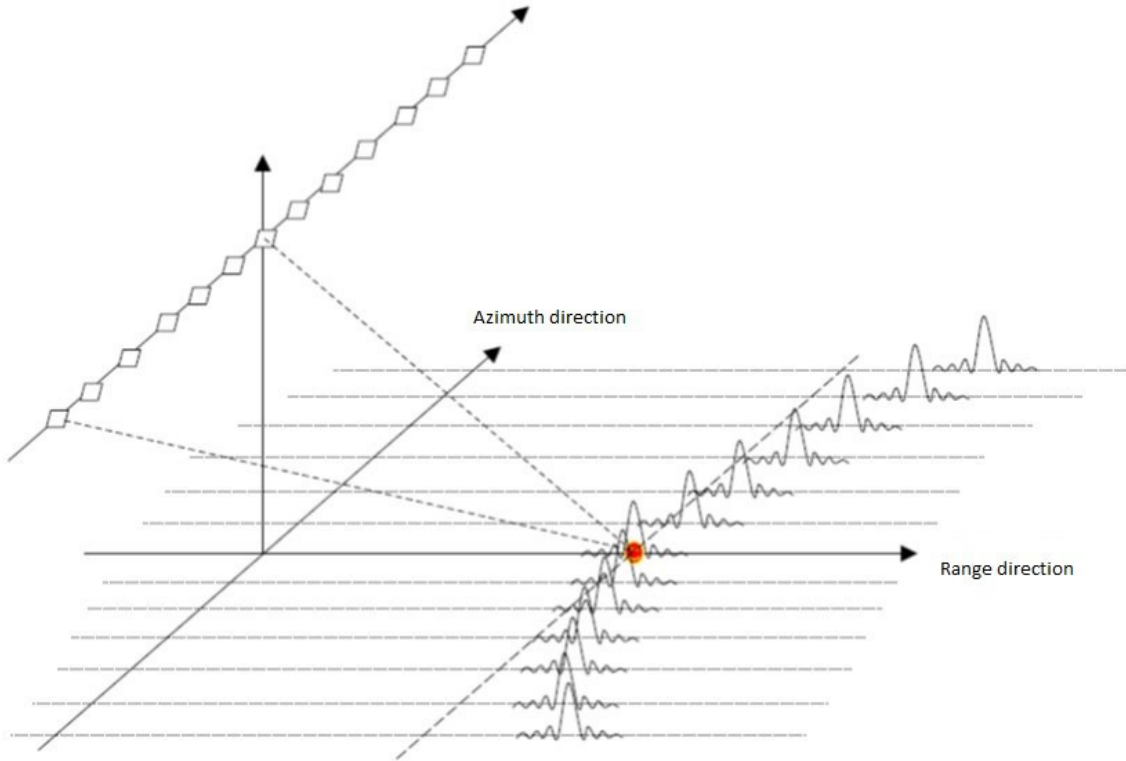

Figure 3.2: Signal diagram after range compression [1].

The diagram of signals after range compression is shown in Figure 3.2. The diagram depicts that the signal trajectory of the azimuth direction is curving, which is not in a same range cell. Due to the variation of slant range between the radar and the target, all reflected signals from the target cannot come in a same range cell and follow a hyperbolic trend in the azimuth direction called the range cell migration (RCM). These signals are required to migrate back to a same range cell, which is called range cell migration correction (RCMC).

In the azimuth time domain, the RCM curves of different targets are different and we cannot correct them at the same time. However, in the azimuth frequency domain, RCM curves of targets with same range distance are same and we can correct them at the same time. This is the reason why the RCMC is performed in the range-Doppler domain [12] [2].

For the low squint cases, the antenna beam points close to zero Doppler direction (side-looking model points to zero Doppler direction). The slant range can be approximated to

$$R(\eta) = \sqrt{R_0^2 + V_a^2 \eta^2} \approx R_0 + \frac{v_a^2 \eta^2}{2R_0} \tag{3.2}$$

Combining Equation (3.1) and (3.2), the range compressed signal can be given by

$$s_{rc}(\tau, \eta) \approx A_0 p_\tau [\tau - \frac{2R(\eta)}{c}] w_a(\eta - \eta_c) exp\{-j\frac{4\pi f_c R_0}{c}\} exp\{-j\pi \frac{2v_a^2}{\lambda R_0} \eta^2\} \tag{3.3}$$

According to Equation (2.20), the second exponential phase term in Equation (3.3) can be expressed by $exp\{-j\pi K_a \eta^2\}$. It is apparent that this phase term is quadratic phase and is a function of η^2. Then, an azimuth FFT is performed on each range gate to transform the range compressed signal into the range-Doppler domain. The relationship between the azimuth time and the azimuth frequency is

$$f_\eta = -K_a \eta \tag{3.4}$$

By substituting Equation (3.4) into Equation (3.3), the data after

37

azimuth FFT in the range-Doppler domain can be given by

$$S_1(\tau, f_\eta) = FFT\{s_{rc}(\tau, \eta)\}$$

$$= A_0 p_r[\tau - \frac{2R_{rd}(f_\eta)}{c}]W_a(f_\eta - f_{\eta_c})exp\{-j\frac{4\pi f_c R_0}{c}\}exp\{j\pi\frac{f_\eta^2}{K_a}\}$$

$$(3.5)$$

where $W_a(f_\eta - f_{\eta_c})$ is azimuth beam pattern in the range-Doppler domain, the first exponential phase term is the inherent phase information of target and the second phase term is the azimuth modulation. The RCM curve is the term $R_{rd}(f_\eta)$ and can be approximated by

$$R_{rd}(f_\eta) \approx R_0 + \frac{v_a^2}{2R_0}\left(\frac{f_\eta}{K_a}\right)^2 = R_0 + \frac{\lambda^2 R_0 f_\eta^2}{8v_a^2} \qquad (3.6)$$

The amount of RCM needed to correct is given by the second term in Equation (3.6).

$$\Delta(f_\eta) = \frac{\lambda^2 R_0 f_\eta^2}{8v_a^2} \qquad (3.7)$$

There are two main approaches to implement the RCMC, which are the nearest neighbour interpolation and the sinc function based interpolation. The nearest neighbour interpolation performs more efficiently but only obtains approximate correction. The efficiency of the sinc function based interpolation depends on the size of interpolator kernel. Longer interpolator kernel can correct more accurately but with a lower efficiency. Usually, a four-point or eight-point interpolation is chosen to give a reasonable accuracy [50].

In Figure 3.3, the signal diagram is corrected and becomes parallel with the azimuth direction. There are many sinc function diagrams which are parallel in the direction of azimuth. This does not mean
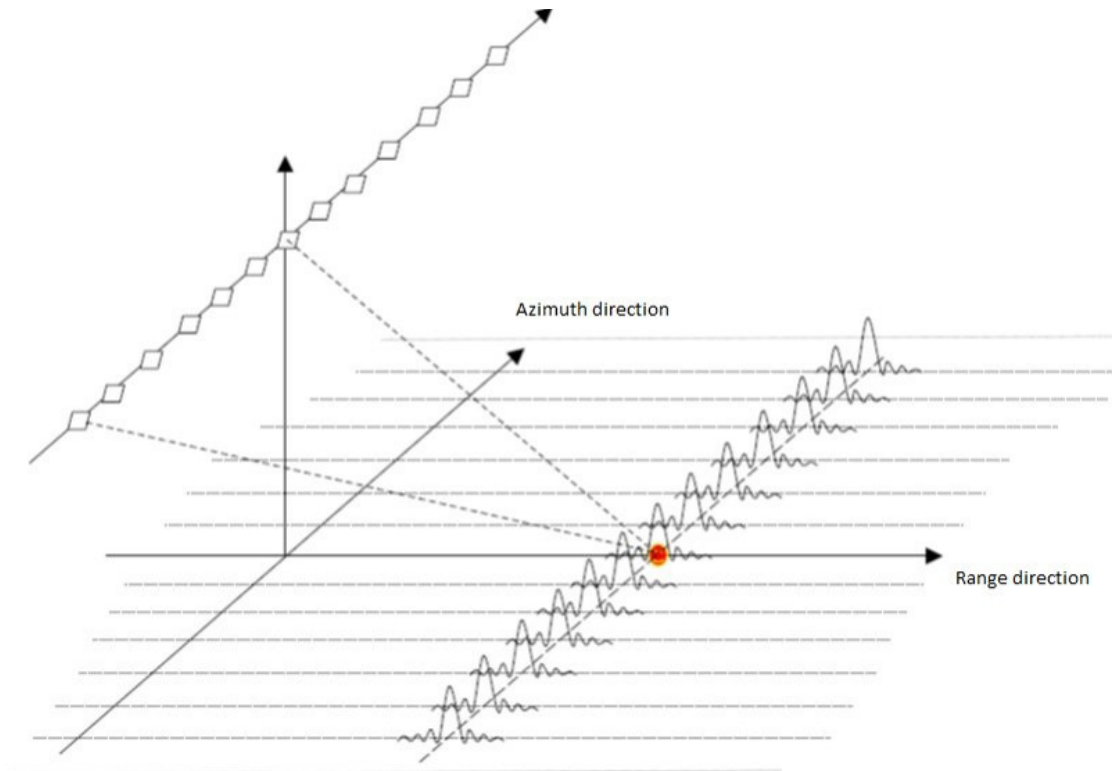
Figure 3.3: Signal diagram after the RCMC [1].

that there are many replicas in the direction of azimuth. It means that the signal data can be seen as a sinc function in the range direction after range compression, which is the processing result of the first step of the range-Doppler algorithm. All data except the columns that are close to the point target in the azimuth direction can be seen as zero if we ignore the effect of noise. This means that the final image will be all black (no reflection) in these areas with data of zero. This is because that the LFM signal in the range direction has been compressed into the sinc function. In the columns that is close to the point target, they will be intensity of the mainlobe and sidelobes of the sinc function in the range direction after the range compression.

Assuming the RCMC is applied accurately, the signal after the RCMC can be represented by

$$S_2(\tau, f_\eta) = A_0 p_r(\tau - \frac{2R_0}{c}) W_a(f_\eta - f_{\eta_c}) exp\{-j\frac{4\pi f_0 R_0}{c}\} exp\{j\pi\frac{f_\eta^2}{K_a}\}$$
(3.8)

It is apparent that the range envelope sinc function p_r becomes independent of the azimuth frequency, which means the RCM has been corrected.

After the RCMC, a matched filter is used to implement the azimuth compression in the azimuth direction to complete pulse compression in the azimuth direction. It is convenient to implement azimuth compression in the Range-Doppler domain. Similar with the matched filter in the range direction, the azimuth matched filter is the complex conjugate of the second exponential phase term in Equation (3.5) to remove quadratic phase in the azimuth direction and can be given by

$$H_{az}(f_\eta) = exp\left\{-j\pi\frac{f_\eta^2}{Ka}\right\}$$
(3.9)

where Ka is the azimuth linear FM rate shown in Equation (3.4). An IFFT is then completed after the azimuth compression. The final signal is given by

$$s_{ac}(\tau, \eta) = IFFT_\eta\{S_2(\tau, f_\eta)H_{az}(f_\eta)\}$$
$$= A_0 p_r(\tau - \frac{2R_0}{c})p_a(\eta)exp\left\{-j\frac{4\pi f_c R_0}{c}\right\} exp\{j2\pi f_{\eta_c}\eta\}$$
(3.10)

where p_a is azimuth impulse response, which is a sinc-like function and similar with p_r. The envelopes p_a and p_r show that the target is

focused and positioned at $\tau = 2R_0/c$ and $\eta = 0$. These two envelopes are orthogonal, which is shown in Figure 3.4, so that we can acquire a focused point in the image space. There are two exponential phase terms in Equation (3.10). The first term is target phase which depends on range position and the second term is a linear phase which depends on the Doppler centroid [13] [12].
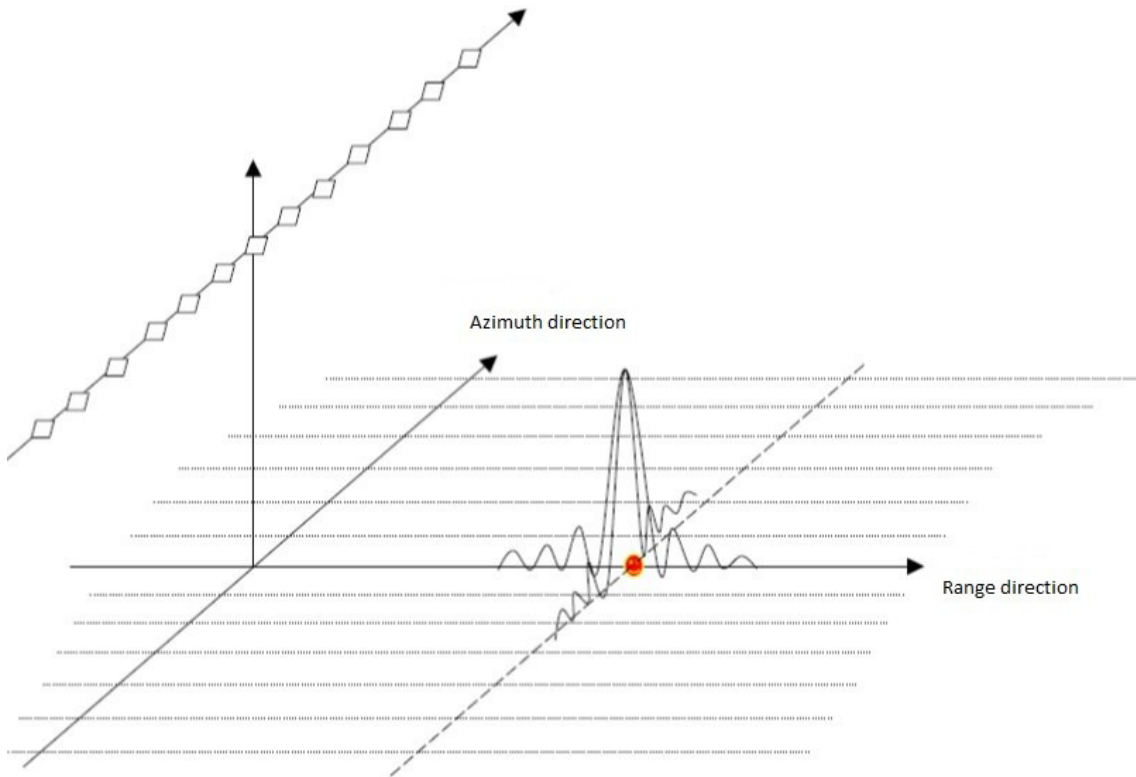

Figure 3.4: Signal diagram after the azimuth compression [1].

Compared with Figure 3.3, Figure 3.4 shows the final SAR image of a point target by using the processing algorithm of the range-Doppler algorithm. In Figure 3.3, the data is a sinc function in the range direction. However, the data in the azimuth direction is still LFM signal with a rate of K_a. It is difficult to show this in a diagram but we can

know it from the Equation (3.8). In Figure 3.4, the LFM signal in the azimuth direction is compressed to the sinc function as well. Hence, the final SAR image shows two orthogonal sinc functions in the position of point target. This means that all data except the column and row of the point target should be zero in theory. The final image of a point target in the SAR image space should be a cross which has a centre in the position of the point target.

3.1.2 Simulation Results

Firstly, a simulation sample of the range-Doppler algorithm is given to acquire a point in the image space. In this simulation, the observation area is from $X_{min} = -400m$ to $X_{max} = 400m$ in the azimuth direction. The central line of observation area in the range direction is $Y_c = 10000m$ and the area in the range direction is from $Y_c - Y_w = 9400m$ to $Y_c + Y_w = 10600m$. The moving velocity of platform is $v = 100m/s$ and the height is $H = 5000m$. The resolution of range and azimuth direction are both set to $\rho_r = \rho_a = 2m$. The sampling points in the azimuth and range direction are $N_a = 2048$ and $N_r = 1024$. The coordinate of target point is $(0, Y_c)$, which is the center location of the observation area.

Figure 3.5 shows the intensity of the point target. In Figure 3.5, high intensity is represented by yellow and low intensity is represented by blue. From this figure, we can find that the location of point tar-

get has a high amplitude intensity. However, there are also many sidelobes in the surrounding locations in the both azimuth and range directions. These sidelobes could make the image distorted. If another point target with low intensity is on the adjacent location of this high intensity point target, the point with low intensity will be covered by the sidelobe of the high value point because the intensity of sidelobe could be higher than the low value point target. This situation will make the processed image distorted and the image could be different from the real image of ground.
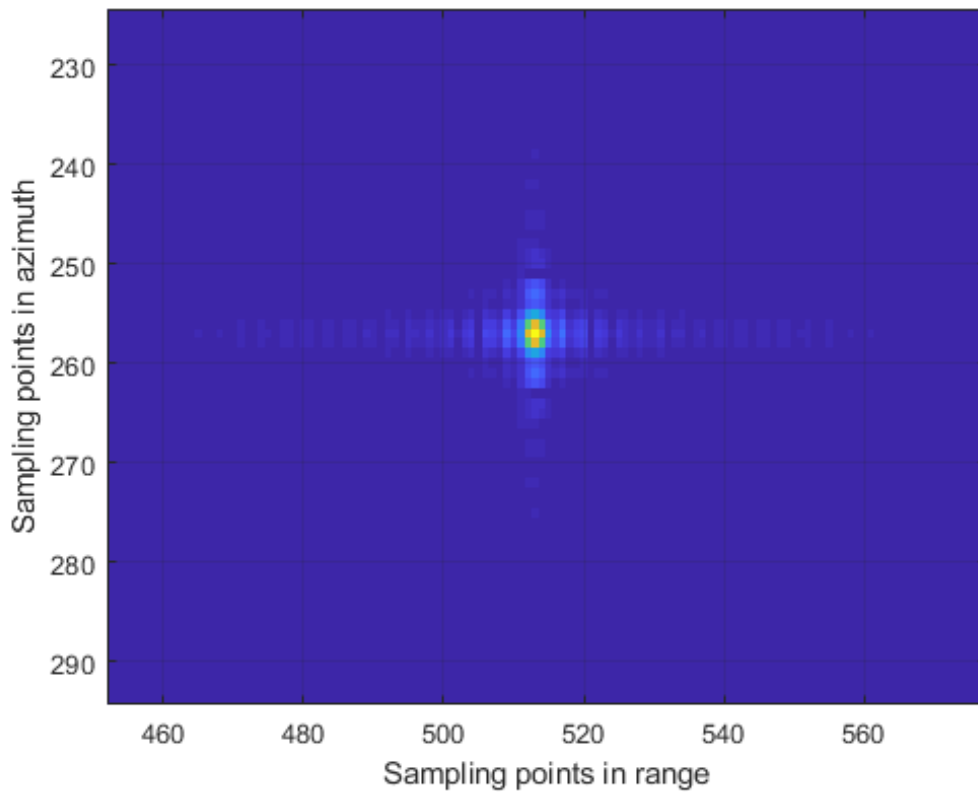

Figure 3.5: Intensity of the point target.

Figures 3.6 and 3.7 show the impulse response (point target result)

in the range and azimuth directions, respectively. In these two figures, we can analyze the performance of this range-Doppler algorithm. The 3dB width of main lobe is the real resolution of this image. From these two figures, the azimuth resolution is 3m and the range resolution is 3.5m. Compared with theoretical resolution 2m, the real resolution of processed image is worse than theoretical calculation. This means that the quality of processed image could be worse than expected. SAR has a ratio to analyze the performance of sidelobe effect, which is called the peak sidelobe ratio (PSLR). It is a ratio of maximum intensity of mainlobe and maximum intensity of strongest sidelobe. In these two figures, the PSLR values of the range and azimuth direction are provided, which are -12.68dB in the range direction and -12.90dB in the azimuth direction. These two values of PSLR are acceptable and this means that we can obtain a clear SAR image. The simulation of an area target is introduced in the following part.
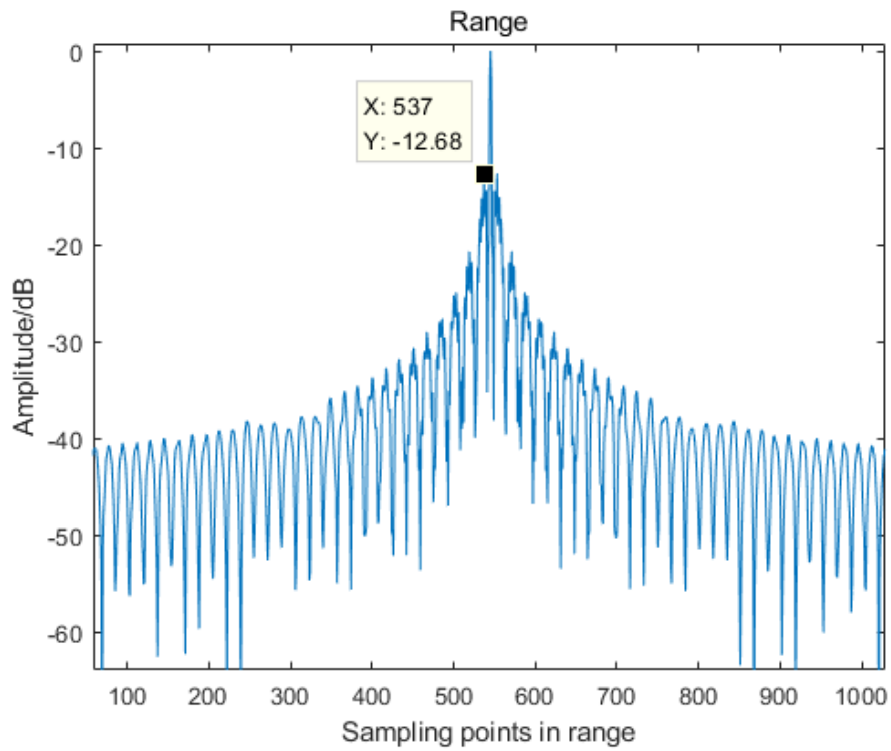
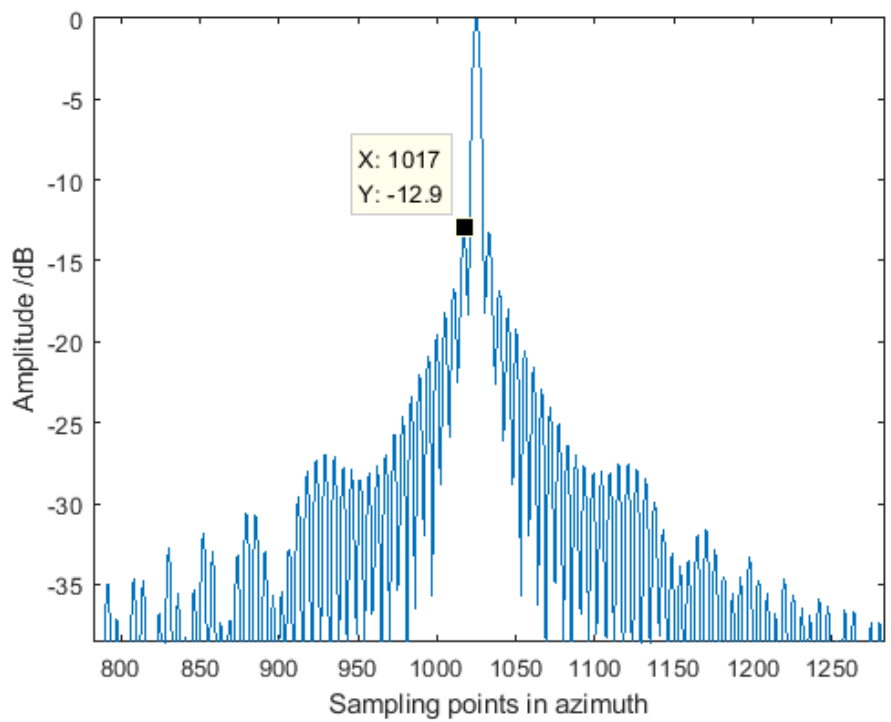Figure 3.6: Impulse response (point target result) in the range direction.

Figure 3.7: Impulse response (point target result) in the azimuth direction.

Secondly, a simulation of area target is shown as follows. A picture or photo is created by many discrete pixels (points with different grayness degrees). Similarly, the area target is equivalent to many point targets with small distance which is smaller than resolution. In this simulation, the observation area in the azimuth direction is still $X_{min} = -400m$ and $X_{max} = 400m$. The observation in range direction is from $Y_c - Y_w = 9400m$ to $Y_c + Y_w = 10600m$, which are all the same as the point target simulation. Other parameters are also the same as the simulation of point target. However, the sampling points of the azimuth and range direction are changed to $N_a = 512$ and $N_r = 1024$. A Google satellite map photo is set in the center area of observing area, which has a size of 601x701, which is shown in Figure 3.8. This means that there are totally 421301 discrete point targets with adjacent distance of half of theoretical resolution, which is 1m. These point targets build a rectangular area target on the center area of observing area. Different point target has different back-scattered reflection coefficient, which is correspond to the grayness degree of pixel in the map photo. Other locations in the observation area all have no target with no reflections. This means that these area will be all black in the processed SAR image.

Figure 3.9 shows the simulation result of the area target. From this image, many details of input image can be distinguished. However, it is obvious that the quality of this reconstructed image is worse than the input image in Figure 3.8. This is because the real resolution of

this image is worse than the theoretical resolution. Also, the quality of image is influenced by the effect of side lobes. This area target simulation result is the same as the analysis of the point target (impulse response) in the above part.
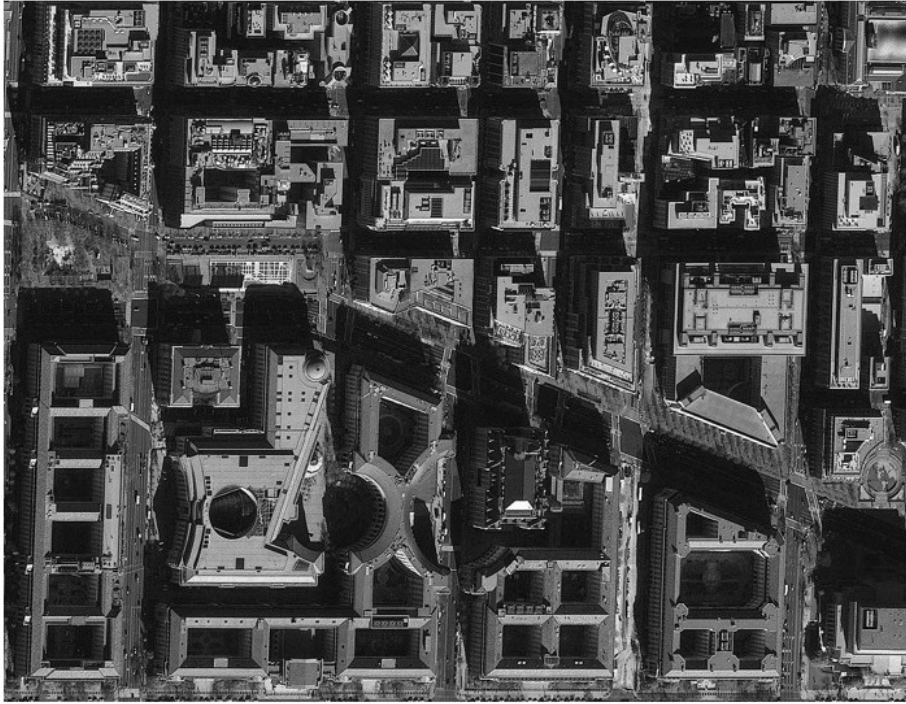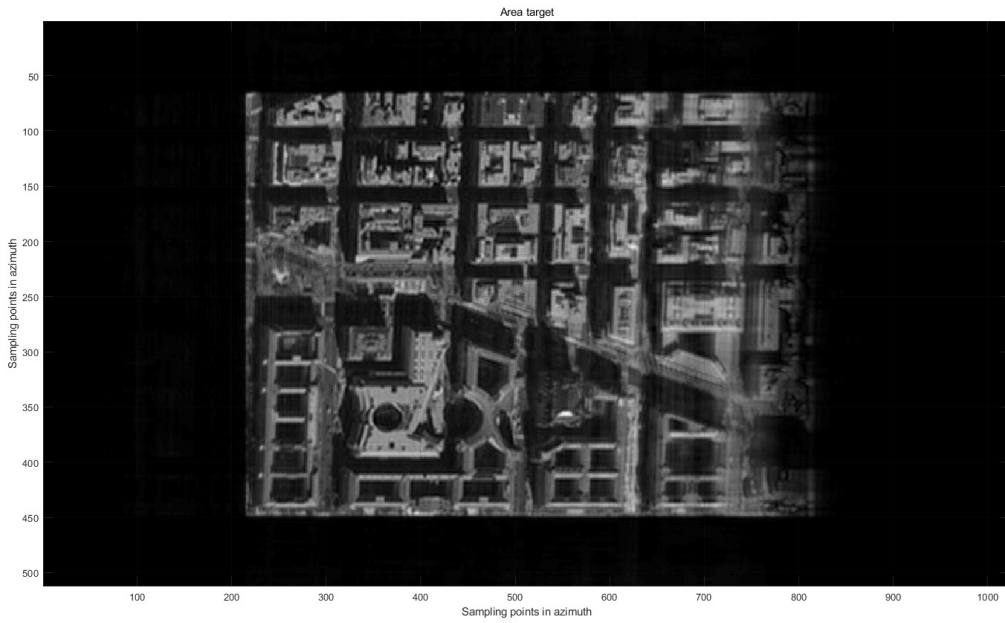
Figure 3.8: Input image of the area target [49].

Figure 3.9: Intensity of the area target.

3.2 Co-prime SAR Concept and Simulations

3.2.1 Introduction to Co-prime Array and CopSAR

In this research, the most significant aim is to reduce the amount of raw data. We can use the concept of sparse array in the array signal processing. The sparse array is a concept which is different from the ULA. The ULA has fixed distance between two adjacent sensors. However, the sparse array has different distance between different two sensors. This means that sparse array uses fewer sensors than the ULA in a same length of array. We can exploit the second order statistical information to receive a smaller performance compared with the ULA. However, the amount of data decreases because the amount of sensors decreases. The co-prime array uses two co-prime integers in two sub-arrays. In Figure 3.10, for two sub-arrays with two co-prime integers, they share the same sensor in the first position and they will share the same sensor again until the $MN - th$ position because M and N are co-prime. This means that we can generate an virtual array with consecutive integers from -M(N-1) to M(N-1), which is a larger virtual ULA with better performance. This is why we are going to utilize the co-prime array in SAR as well.

The concept of co-prime array will be introduced in deails in the following parts. Co-prime array is one kind of sparse arrays. The co-prime array consists of two uniform linear sub-arrays with distance Md and Nd respectively, which is shown in Figure 3.10. There are

49

M sensors in the first sub-array and N sensors in the second sub-array where M and N are co-prime integers, for example, 4 and 5. In the location of 0, two sub-arrays share same sensor. Except this sensor, two sub-arrays have separate ULA pattern with different spacing. d is the unit of inter-element spacing. For uniform linear array (ULA), d is typically set to $\lambda/2$ or smaller than $\lambda/2$ to avoid spatial aliasing [51] [54]. However, it is obvious that distance between two adjacent sensors of the co-prime array is larger than d.

Based on the sparse array signal processing, we can build an virtual ULA. Based on the concept of difference co-array, an virtual ULA with $2M(N-1)+1$ virtual sensors can be generated. The virtual sensors are corresponding to the consecutive integers from $-M(N-1)$ to $M(N-1)$. This operation leads to a significant increase in the degrees of freedom, which means co-prime array can receive same performance with fewer sensors (fewer sampling points and fewer amount of data in SAR) [51].
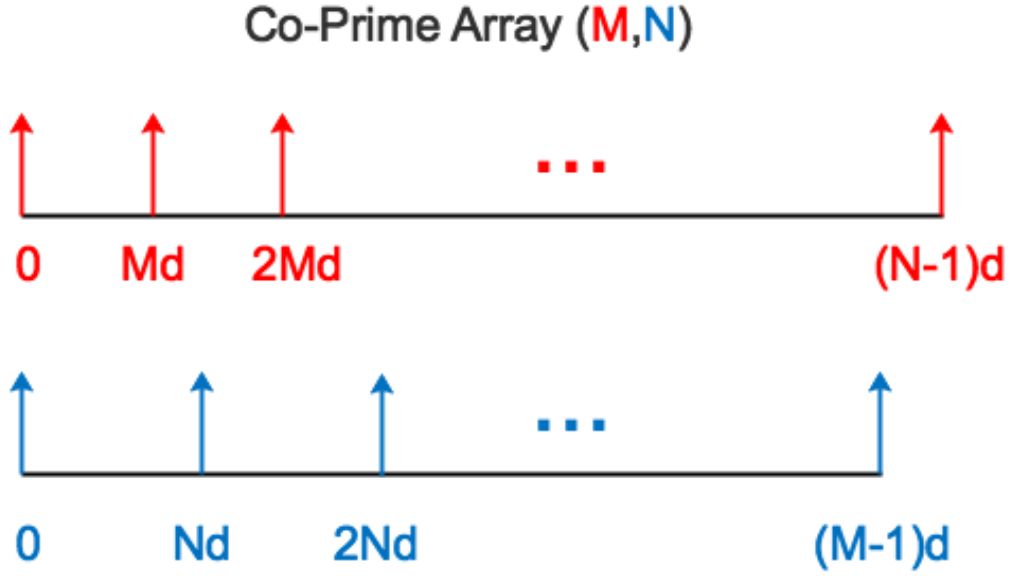
Figure 3.10: A general co-prime array structure.

For the co-prime SAR, it uses the concept of co-prime to reduce the sampling points, which reduces the amount of the raw data stored and increase the range swath [16]. Because this approach is still based on matched filter, the sampling must obey the Nyquist sampling theorem. This means that the sampling frequency must higher than the bandwidth of signal. In the azimuth direction, the bandwidth is the SAR signal Doppler bandwidth, i.e., its Nyquist rate. Usually, in order to avoid the aliasing, the selected PRF of conventional SAR must be larger than the Doppler bandwidth, which can be represented as

$$PRF_0 \geq \frac{2v}{L} \tag{3.11}$$

where v is the velocity of SAR platform and L is the real length of antenna. However, the PRF of co-prime array must be smaller than the PRF_0 because the distance between two adjacent sensor increases.

51

For example, if the two co-prime integers are 4 and 5, the structure of CopSAR are shown in Figure 3.11. The blue point is the first sub-array with $M = 4$, which means its $PRF_1 = PRF_0/M$. The other red points are the second sub-array with $N = 5$ and the $PRF_2 = PRF_0/N$. Because two integers are co-prime, the array will repeat the pattern each $MN = 20$ sensors. To calculate the reduction of raw data, a ratio R is defined between the number of pulses transmitted by the CopSAR and the number of pulses transmitted by the conventional SAR. The ratio R can be expressed as

$$R = \frac{1}{PRF_0}(\frac{PRF_0}{M} + \frac{PRF_0}{N} - \frac{PRF_0}{MN}) = \frac{M + N - 1}{MN} \quad (3.12)$$

Figure 3.11: Structure of the CopSAR concept.

The PRF of CopSAR is lower than the Nyquist rate, the replica ghost targets will be displayed on the image space. The shift of replicas in the azimuth direction and the range direction can be calculated by the following equations:

$$\Delta x_i = i\frac{PRF_0\lambda r_0}{2v} \quad (3.13)$$

$$\Delta r_i = \frac{\Delta x_i^2}{2r_0} \quad (3.14)$$

where λ is the wavelength, r_0 is the closest slant range between the radar and the target. Two sub-arrays can be used to produce two separate SAR images. This means that they should use different PRF

to calculate replicas in different SAR images. For the first sub-array, each target gives rises to replicas displayed as

$$\Delta x_{i1} = i_1 \frac{PRF_0 \lambda r_0}{M2v} \tag{3.15}$$

$$\Delta r_{i1} = \frac{\Delta x_{i1}^2}{2r_0} \tag{3.16}$$

For the second sub-array, each target gives rise to replicas displayed as

$$\Delta x_{i2} = i_2 \frac{PRF_0 \lambda r_0}{N2v} \tag{3.17}$$

$$\Delta r_{i2} = \frac{\Delta x_{i2}^2}{2r_0} \tag{3.18}$$

The resolution of these two processed images are the same as the conventional SAR because the synthetic array length of CopSAR is the same as the conventional SAR. But because of the low sampling frequency, these two images are severely aliased. According to aforementioned equations, replicas on the two images will at different locations, unless it is the real target. To combine these two aliased images, we can choose the smaller modulus at each pixel, the replica ghost targets will be removed. The choosing step can be represented as

$$s(x,r) = \begin{cases} s_1(x,r), if |s_1(x,r)| < |s_2(x,r)| \\ s_2(x,r), otherwise \end{cases} \tag{3.19}$$

Because this CopSAR is used in the scenario of ocean ships detection, a replica in the location of one aliased image, the same location of another aliased image must be dark and without any replica. The final image $s(x,r)$ with no replica can be obtained. In one of the two aliased

images, there is a replica ghost of the target. In the other aliased image, it should be darkness with low modulus (sea background). By choosing the smallest modulus of the two aliased images, the replica ghost targets can all be removed. Some simulation results of CopSAR are shown in the following subsection.

3.2.2 Simulation Results

Firstly, a simulation of single point target is provided. The parameters are the same as the area target simulation in the section 3.1.2. The two co-prime integers are the same as the aforementioned example, which are 4 and 5. The conventional SAR $PRF_0 = 94.858Hz$. The PRF of two sub-arrays are $PRF_1 = 23.7145Hz$ and $PRF_2 = 18.9716Hz$, respectively. These two PRF are lower than Nyquist rate and will result in severely aliased. The point target is set on the center of observing area, which is (0,Yc). The aliased image $s_1(x, r)$ is created by the first sub-array and the $s_2(x, r)$ is created by the second sub-array. The final image $s_{12}(x, r)$ is created by combining $s_1(x, r)$ and $s_2(x, r)$ using the smallest modulus of each pixel.
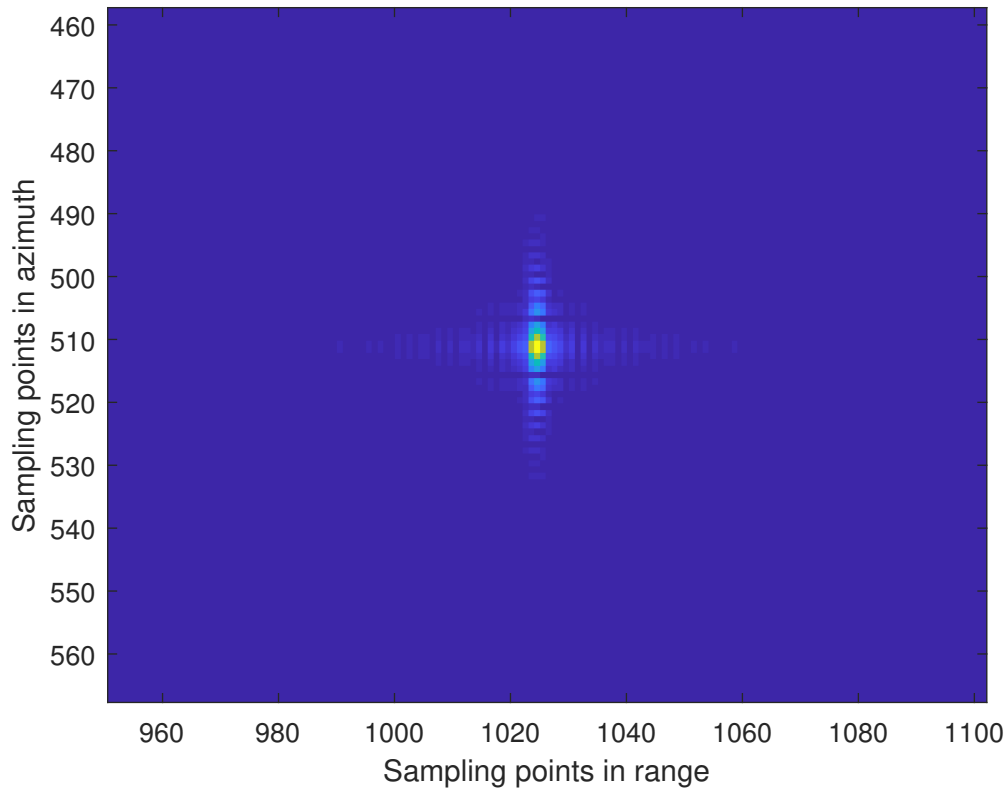
Figure 3.12: Intensity of point target processed by the CopSAR.

In Figure 3.12, a point target processed by CopSAR is shown. Compared with simulation result of conventional SAR, it has similar performance of resolution and side lobes. However, the amount of data decreases significantly compared with conventional SAR. In the conventional SAR, the sampling points of this simulation is 1024. For this CopSAR, the number of sampling points in the first sub-array is 256 and the number is 205 in the second sub-array. This means that there are 461 sampling points totally. This is a significant reduction compared with the conventional SAR. Because the PRF reduces, the range swath also increases without any loss of geometric resolution.

Figures 3.13 to 3.16 show the impulse response (point target result) of the first sub-array aliased image, the second sub-array aliased image, the combined image and the conventional SAR image, respectively. According to Figures 3.13 and Figure 3.14, it is obvious that the location of replica ghost targets are different for different sub-arrays. Hence, by choosing the smallest modulus of each pixel, we can achieve the final image in Figure 3.15. Compared with the image of conventional SAR, it has small sidelobes around the point target but it can be ignored because it is relatively much lower than the mainlobe of the point target. This means that this approach CopSAR can achieve similar performance of image quality but with a significant reduction of data amount and increase of range swath.
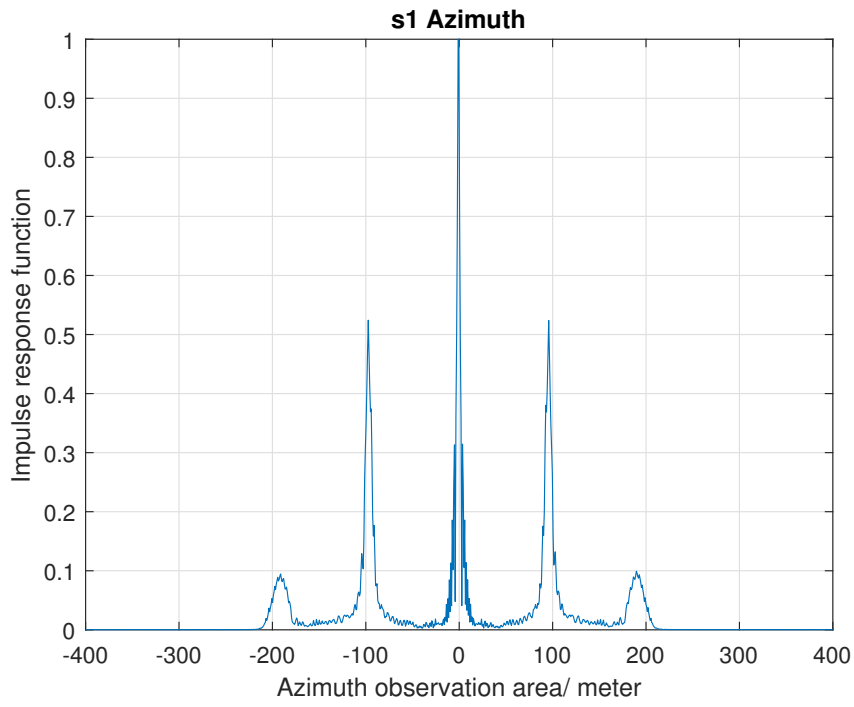
Figure 3.13: Impulse response (point target result) of $s_1(x, r)$ in the azimuth direction.
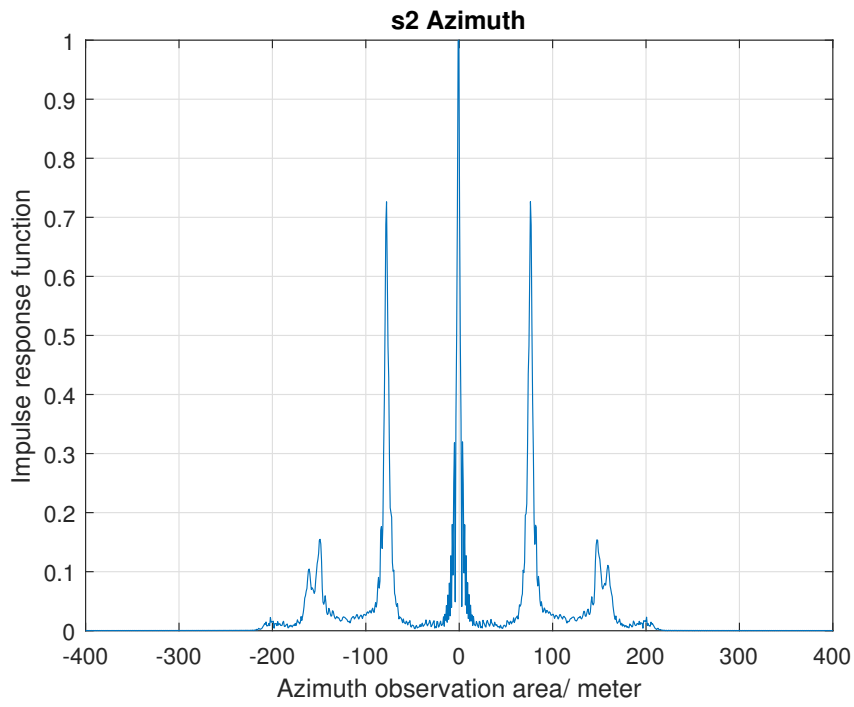

Figure 3.14: Impulse response (point target result) of $s_2(x, r)$ in the azimuth direction.
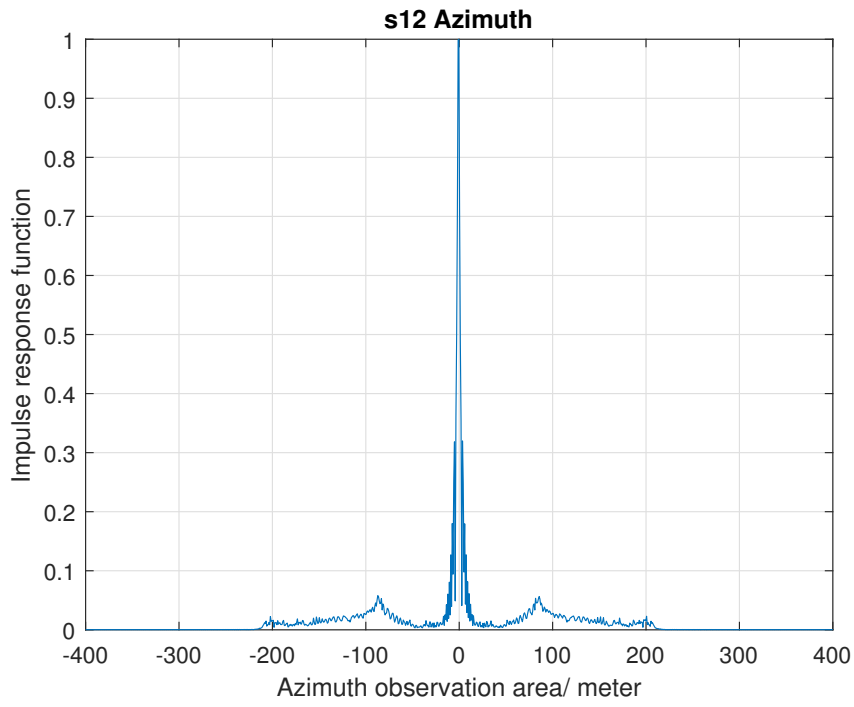
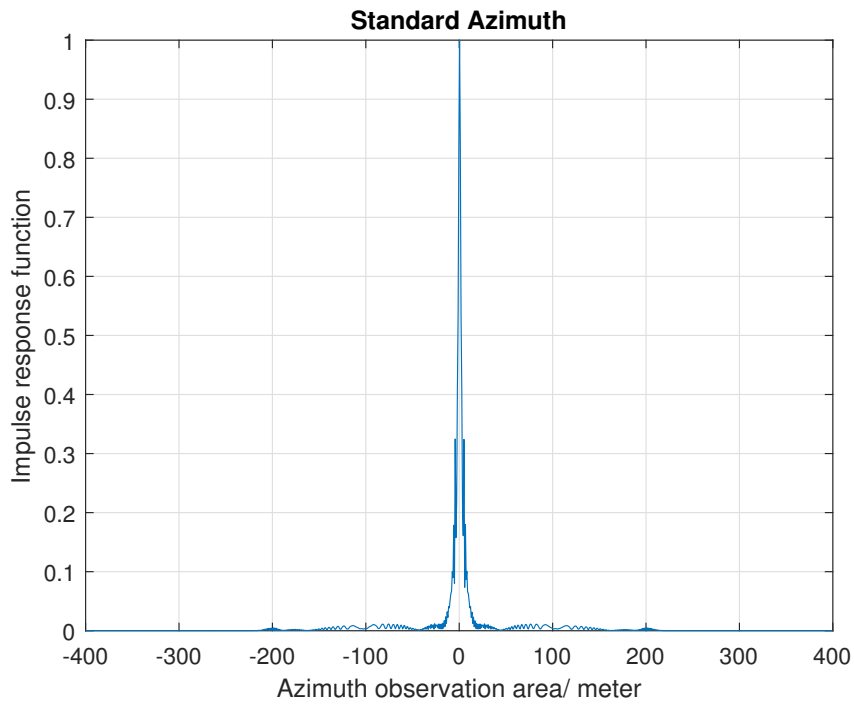Figure 3.15: Impulse response (point target result) of $s_{12}(x, r)$ in the azimuth direction.

Figure 3.16: Impulse response (point target result) of the conventional SAR in the azimuth direction.

The second simulation is to simulate a ship target with length of 100m, which is a long target with many point targets. The parameters of simulation are all the same as the point target simulation. In Figures 3.17 and 3.18, the simulation results of CopSAR and conventional SAR are compared.

Compared with the point target simulation result of the conventional SAR, the result of CopSAR has some small replicas in the image. This is because the replica ghost targets also have sidelobes. Some replica sidelobes of these two aliased images coincide in the same locations and cannot be removed perfectly. This situation results in that the replica ghost targets cannot be remove completely using the approach of Equation (3.19). However, the modulus is much lower compared with the real target and can be ignored and seen as noise in the final image. Furthermore, we can compare the data amount of this two approaches. The conventional has 1024 sampling points. The CopSAR has 256 sampling points in the first sub-array and 205 sampling points in the second sub-array. There are only 461 sampling points totally in the CopSAR, which is only 45% of the data amount in the conventional SAR. It is obvious that the CopSAR has a better advantage of data amount in some scenarios (ship detection and surveillance in the ocean).
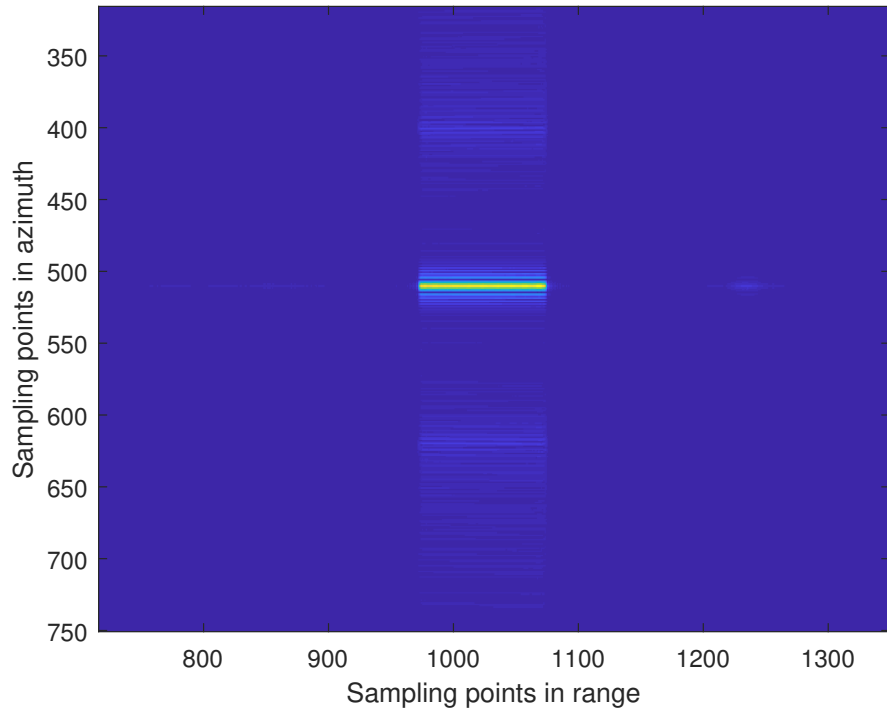
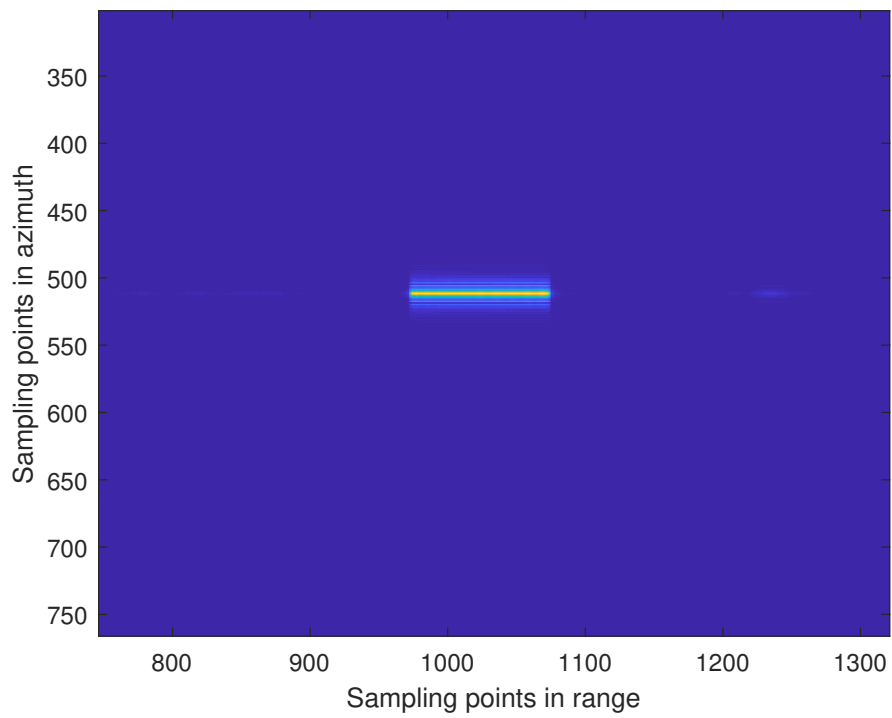Figure 3.17: Intensity of ship target processed by the CopSAR.

Figure 3.18: Intensity of ship target processed by the conventional SAR.

Chapter 4

Least Squares Beamforming Based Processing Method

4.1 Conventional Beamforming Method with Windows

4.1.1 Conventional Beamforming Based SAR Processing Method

In the last chapter, the expression of point target in the azimuth direction is represented in Equation (2.22). The matched filter method, such as the most commonly used range-Doppler algorithm, is to remove quadratic phase of the signal and compress the chirp signal into a sinc function in the azimuth direction so that we can obtain a clear image of the point target [2]. The matched filter method performs pulse compression in the Fourier transformed azimuth domain for a higher processing time efficiency. The Fourier transform is processed using fast Fourier transforms (FFTs). For the range-Doppler algorithm, the signals of azimuth direction are transformed into the frequency domain via FFT. After Fourier transform, the expression of point target

in the frequency domain can be expressed as

$$S_1(f_\eta) = A_0 \, W_a(f_\eta - f_{\eta_c}) \, exp\{j\pi \frac{f_\eta^2}{K_a}\} \qquad (4.1)$$

where $Ka = \frac{2v_a^2}{\lambda R0}$ and Ka is the linear FM rate of azimuth signal, which has been shown in Equation (2.20). The matched filter of the azimuth direction is the complex conjugate of the exponential phase term in Equation (4.2). and can be given by

$$H_{az}(f_\eta) = exp\left\{-j\pi \frac{f_\eta^2}{Ka}\right\} \qquad (4.2)$$

The data of point target in the frequency domain is multiplied by the matched filter and then transformed back to the time domain using IFFT to obtain a clear image. For a point target in the azimuth direction in the observation area, the simulation result after processing by the range-Doppler algorithm is shown in Figure 4.1. We can see that the impulse response shows a sinc function with a mainlobe and some sidelobes. The matched filter method is equivalent to the beamforming method. Hence, the impulse response is the same as the result of point target. The width of mainlobe (-3dB width) is 2.1m, which is similar to the theoretical resolution 2m. The value of sidelobe is -13.5dB. Response with high sidelobes could affect the quality of SAR image. For the matched filter method, the value of sidelobe is a main problem which need to be solved.

Compared with Figure 3.7, the performance of mainlobe width and PSLR in Figure 4.1 are better. This is because the result of Figure 3.7 are processed using the 2D raw data with both range and azimuth di-

rections. The sidelobe value PSLR in Figure 4.1 is a theoretical result using the matched filter (conventional beamforming). In the following part, we are going to explain why the matched filter is equivalent to the conventional beamforming under the framework of the array signal processing.

In the view of array signal processing, the process of the matched filter can be seen as beamforming. The collected raw data in the azimuth direction is collected by an virtual ULA. This means that the raw data can be seen as input data in array signal processing and the matched filter can be seen as the weight in different virtual sensors. Assume the collected raw data is X, Equation (2.22) can be expressed in the form of matrix

$$
X = AS = \begin{bmatrix} 0 \\ \vdots \\ 0 \\ exp{-j\frac{4\pi}{\lambda}R_1} \\ exp{-j\frac{4\pi}{\lambda}R_2} \\ \vdots \\ exp{-j\frac{4\pi}{\lambda}R_{n-1}} \\ exp{-j\frac{4\pi}{\lambda}R_n} \\ 0 \\ \vdots \\ 0 \end{bmatrix}_{M\times 1} \begin{bmatrix} \sigma_1 \end{bmatrix} \tag{4.3}
$$

where A is the exponential phase of reflected signal and S is the re-
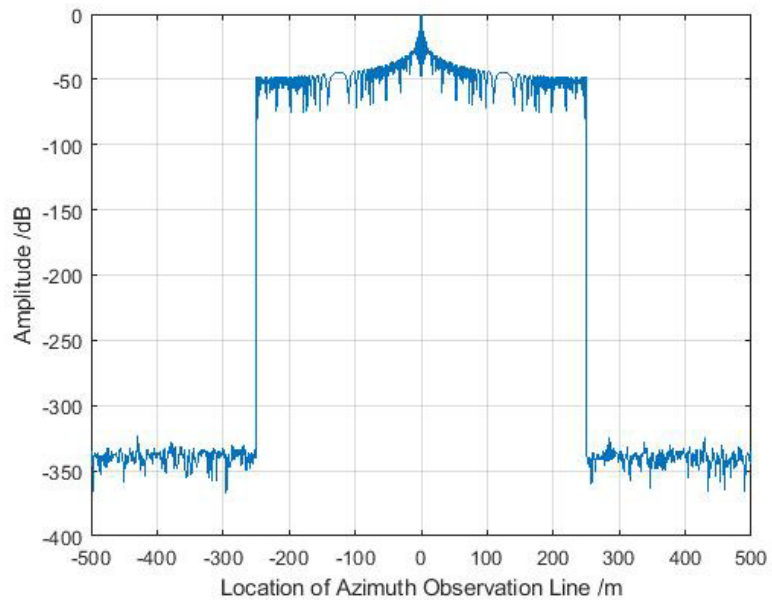
(a) Impulse response (point target result) of matched filter method (the range-Doppler algorithm).
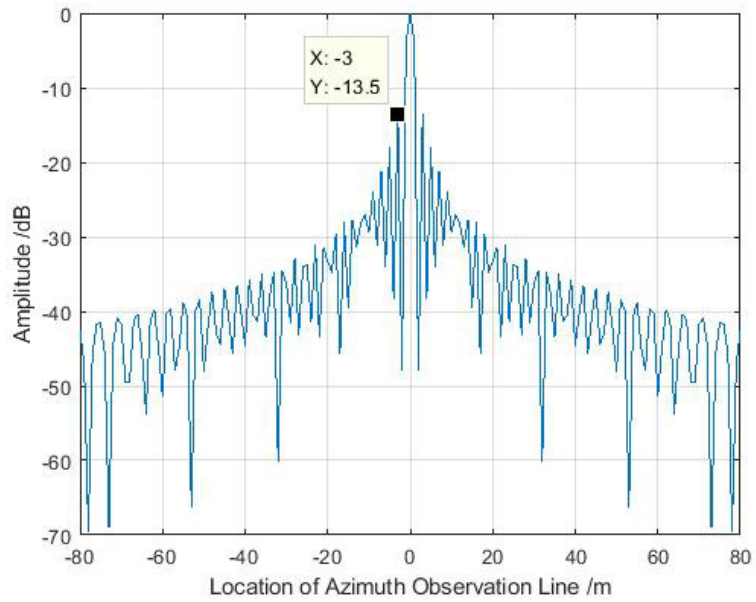
(b) Details of mainlobe and sidelobes.

Figure 4.1: Matched filter method (range-Doppler algorithm).

flection coefficient matrix of point target. In matrix A, we assume the synthetic aperture length has n sampling points. This means that n points can receive the reflected signal from the point target. The raw data X consists of the whole observation line and there are totally M sampling points in matrix X. The entire observation line is much longer than the synthetic aperture length. All other sampling points cannot receive the reflected signal from this point target and there are all zero in other points. This is why only n points of exponential phase part have non-zero data. The R_1 is the first sampling point which receives the reflected signal from the point target. The R_2 is the second sampling and the R_n is the $n - th$ sampling points. The matrix S is the matrix of the point target reflection coefficients. In Equation (2.22), there is only one point target. Hence, the matrix S is a single value of σ_1, where σ_1 is the back-scattered reflection coefficient of the point target.

For more complicated situation, assume there are two point targets in the observation line and the positions of two points have a distance of two sampling points. By using these assumption, we can re-express

the Equation (2.22) into

$$X = AS = \begin{bmatrix} 0 & 0 \\ \vdots & \vdots \\ 0 & 0 \\ exp-j\frac{4\pi}{\lambda}R_{11} & 0 \\ exp-j\frac{4\pi}{\lambda}R_{21} & 0 \\ \vdots & exp-j\frac{4\pi}{\lambda}R_{12} \\ exp-j\frac{4\pi}{\lambda}R_{(n-1)1} & exp-j\frac{4\pi}{\lambda}R_{22} \\ exp-j\frac{4\pi}{\lambda}R_{n1} & \vdots \\ 0 & exp-j\frac{4\pi}{\lambda}R_{(n-1)2} \\ 0 & exp-j\frac{4\pi}{\lambda}R_{n2} \\ 0 & 0 \\ \vdots & \vdots \\ 0 & 0 \end{bmatrix}_{M\times 2} \begin{bmatrix} \sigma_1 \\ \sigma_2 \end{bmatrix} \qquad (4.4)$$

where the R_{11} is the first sampling point received the reflected signal from the first point target and the R_{n1} is the $n-th$ sampling point received the reflected signal from the first point target. In the same pattern, the R_{12} is the first sampling point received the reflected signal from the second point target and the R_{n2} is the $n-th$ sampling point received the reflected signal from the second point target. In the matrix A, the exponential phase data of the second point target is two sampling points after the exponential phase data of the first point target. The expression is the same as our assumption. The matrix S also extends to two rows because of two point targets. The σ_1 is the reflection coefficient of the first point target and the σ_2 is the reflection

coefficient of the second point target. If there are more points targets in the observation line, we can simply extend more columns of matrix A and more rows of matrix S in the Equation (4.3).

In Figure 4.2, a general matrix pattern of SAR raw data is shown. It can be used to express any scenario with any number of point targets. The shadow parts of columns in matrix A are non-zero exponential data of different point targets in observation line, which is similar to the steering vector in the model of array signal processing.
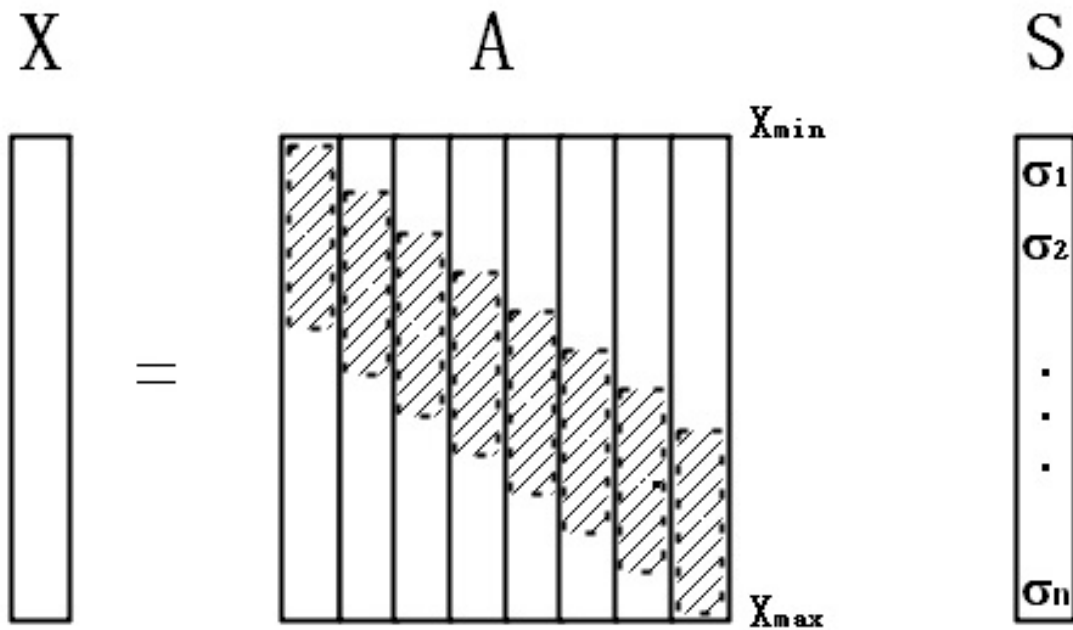

Figure 4.2: General matrix pattern of SAR raw data.

The purpose of processing is to remove the exponential phase part, which is similar to the beamforming method. In beamforming, the data collected by sensors are processed by weight vector to form a

beam pointing to desired direction and suppress interfering signals from other directions [32] [24]. It is convenient to develop matrix notation to express the output after processing. Define a weight vector **w** and raw data vector **X**, then

$$\mathbf{w} = [w_0, w_1, ..., w_{M-1}]^T \tag{4.5}$$

$$\mathbf{X} = [x_0, x_1, ..., x_{M-1}]^T \tag{4.6}$$

where the T is the transpose of matrix. The output of array can be expressed as

$$\boldsymbol{Y} = \boldsymbol{w}^H \boldsymbol{X} = \boldsymbol{w}^H \boldsymbol{AS} \tag{4.7}$$

where the weight vector is the complex conjugate of the exponential phase matrix A and the $\boldsymbol{H}$ is the Hermite transpose of the matrix. By the theory of array signal processing, we can prove that the conventional beamforming method can be utilized in SAR. This processing method is equivalent to the matched filter method. The only difference is that this conventional beamforming method is implemented in the time domain, but the matched filter method (range-Doppler algorithm) is implemented in the frequency domain. Hence, it is obvious that the conventional beamforming can receive similar result (similar mainlobe width and sidelobe value).

In order to improve the performance of procecssing result, we can add windows based on conventional beamforming. A new window weight vector can be added to the data after processing. There are many kinds of windows to control the main beam width and the side-

lobe value. The relationship between width of main beam and the value of sidelobe is a trade-off problem. Smaller main beam width (higher spatial resolution) means higher value of sidelobe. The level of sidelobes is defined as the ratio of peak intensity of mainlobe and the peak intensity of the highest sidelobe, which is called the peak sidelobe ratio (PSLR). A smaller value of PSLR means a better method. The spatial resolution is evaluated by the value of impulse response width (IRW). It is the width of mainlobe of impulse response, which is measured by 3dB width of the mainlobe, or the minimum distance to distinguish two point targets.

In this thesis, five kinds of windows are used for SAR data processing, which are rectangular window, Hanning window, Hamming window, Blackman window and Kaiser window. The expressions of these windows are represented below

$$\text{Rectangular} \quad w(m) = 1, m = 1, 2, ...M \tag{4.8}$$

$$\text{Hanning} \quad w(m) = 0.5(1 - cos\frac{2\pi m}{M}), m = 1, 2, ...M \tag{4.9}$$

$$\text{Hamming} \quad w(m) = 0.54 - 0.46cos\frac{2\pi m}{M}, m = 1, 2, ...M \tag{4.10}$$

$$\text{Blackman} \quad w(m) = 0.42 - 0.5cos\frac{2\pi m}{M} + 0.08cos\frac{4\pi m}{M}, m = 1, 2, ...M \tag{4.11}$$

$$\text{Kaiser} \quad w(m) = \frac{I_0(\beta\sqrt{1-(2m/M)^2})}{I_0(\beta)}, m = 1, 2, ...M \qquad (4.12)$$

where M is the number of sampling points for the entire observation area, I_0 is the zeroth-order modified Bessel function and β the non-negative real number called attenuation coefficient that determines the shape of the window. The attenuation coefficient determines the trade-off between mainlobe width and sidelobe level. Usually, this coefficient is chosen as β=2.5.

According to above equations, it is obvious that the rectangular window is equivalent to processing without window. Hanning, Hamming and Blackman windows all have an increased mainlobe width to obtain a lower value of sidelobe. In these three windows, Hanning obtains the highest PSLR and Blackman obtains the lowest PSLR. For Kaiser window, the sidelobe part of window weight vector is one-third of the mainlobe weight to have a suitable mainlobe width and value of sidelobes.

4.1.2   Simulation Results

In this section, some simulation results are provided. We build a SAR model in MATLAB [47] to create raw data. The observation area is from $X_{min} = -500m$ to $X_{max} = 500m$ in the azimuth direction. The central line of the observation area in range direction is $Y_c = 10000m$. The moving velocity of platform is $v = 100m/s$ and the height is

70

$H = 6000m$. The resolution of the azimuth direction is set to 2m. The sampling points in the azimuth direction is $M = 1001$. The coordinate of target point is $(0, Y_c)$, which is the center location of the observation area. The synthetic aperture length of SAR is $L_{sar} = 250m$. The sampling frequency is $PRF = 100Hz$. This means that the distance between two sampling points(two virtual sensors) is $d = 1m$.

Figures of simulation results are shown below for different windows. For Figure 4.3, it is the response with rectangular window (or without window). The result of this method is equivalent to the matched filter. For Figure 4.3(b), this figure shows the response details of main beam and sidelobes after the conventional beamforming method. The value of PSLR is -13.5dB, which is also similar to the result of matched filter method.

For Figures 4.4, 4.5 and 4.6, it is obvious that the value of PSLR is smaller than the rectangular window. The Hanning, Hamming and Blackman windows show a decreasing trend of PSLR. The values of PSLR are decreasing from -14.26dB (Hanning window) to -14.33dB (Hamming window), then -14.9dB for Blackman window. Figure 4.7 shows the result of conventional beamforming with Kaiser window, which has an attenuation coefficient β=2.5. The value of PSLR is -13.81dB, which is worse than the performance of other windows. However, this method obtains a balance between the mainlobe width IRW and the sidelobe effect PSLR.
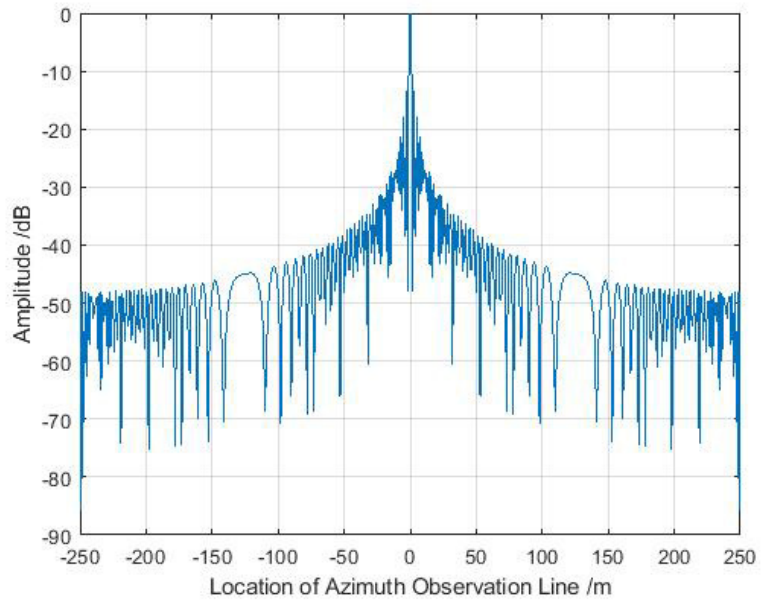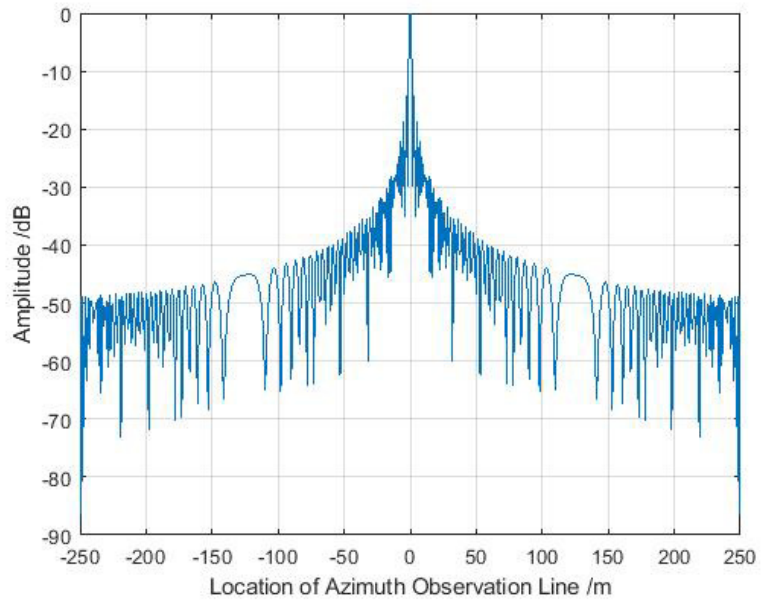
(a) Impulse response (point target result) of conventional beamforming with rectangular window.
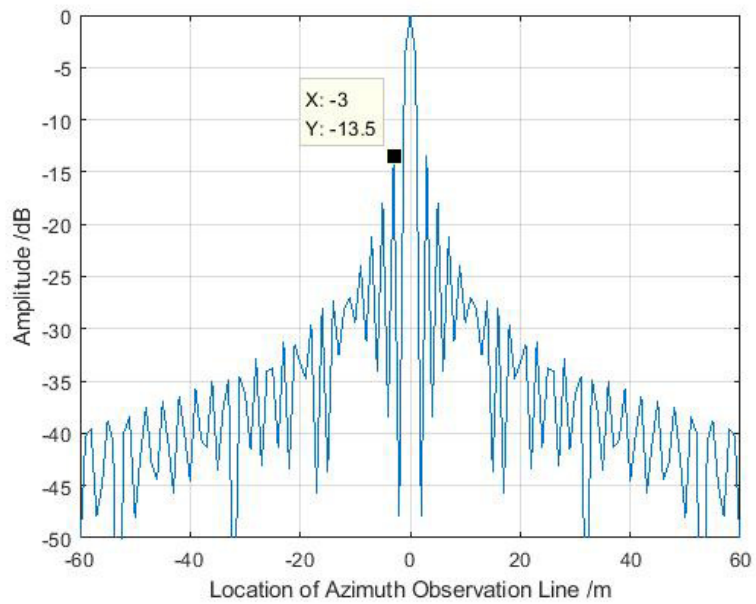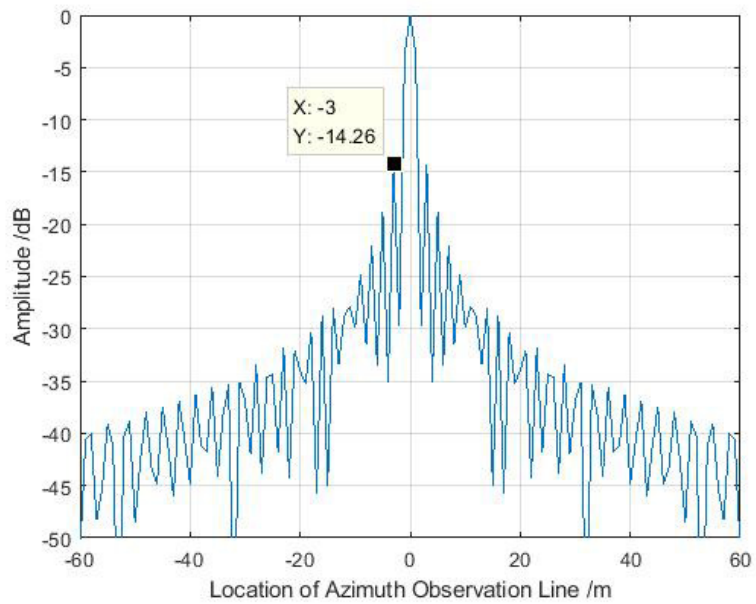

(b) Details of mainlobe and sidelobes.

Figure 4.3: Conventional beamforming with rectangular window.

(a) Impulse response (point target result) of conventional beamforming with Hanning window.

(b) Details of mainlobe and sidelobes.

Figure 4.4: Conventional beamforming with Hanning window.

(a) Impulse response (point target result) of conventional beamforming with Hamming window.

(b) Details of mainlobe and sidelobes.

Figure 4.5: Conventional beamforming with Hamming window.

(a) Impulse response (point target result) of conventional beamforming with blackman window.

(b) Details of mainlobe and sidelobes.

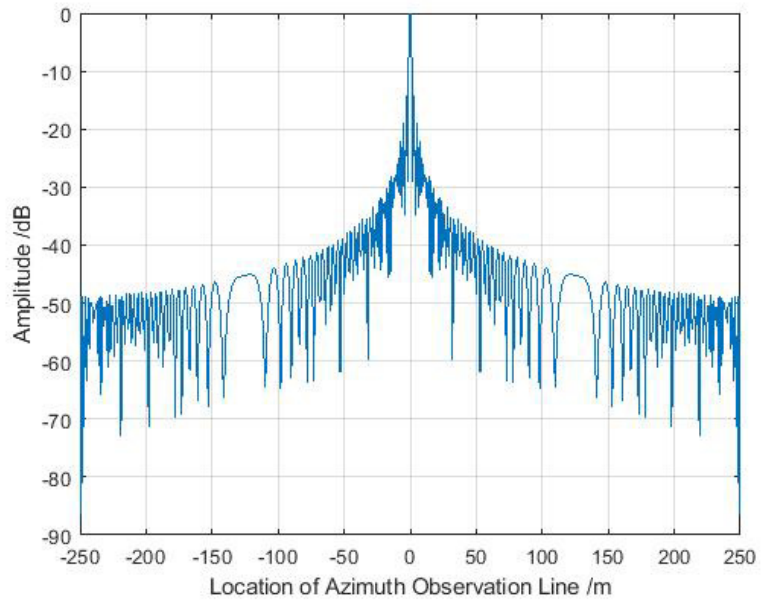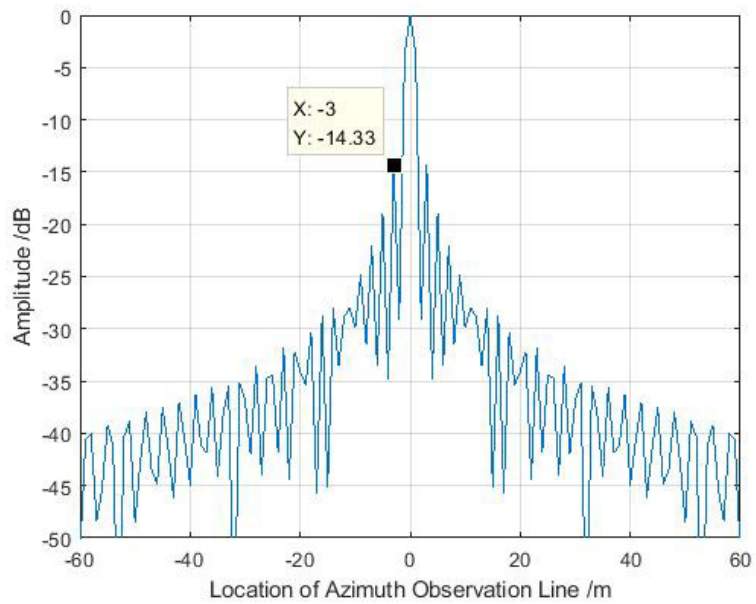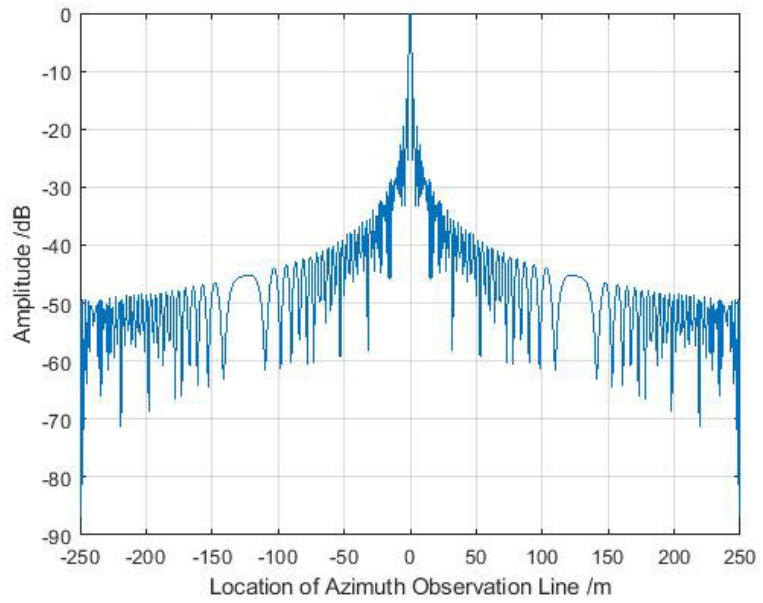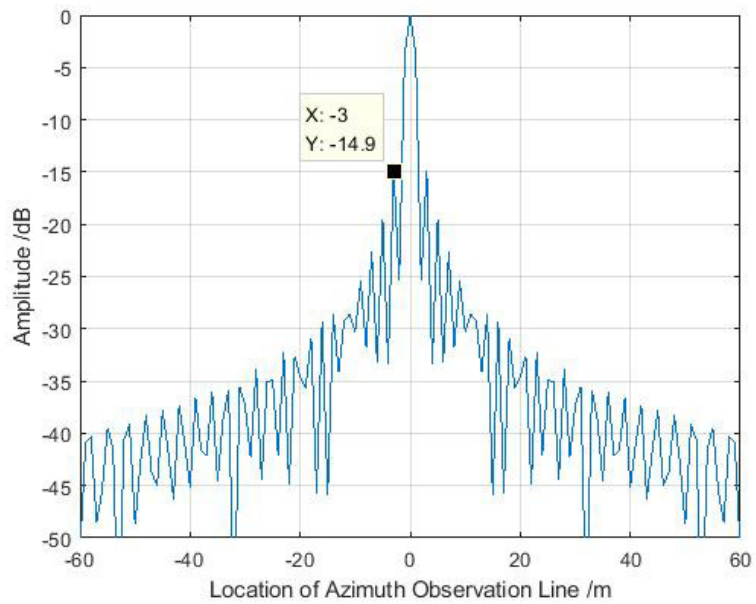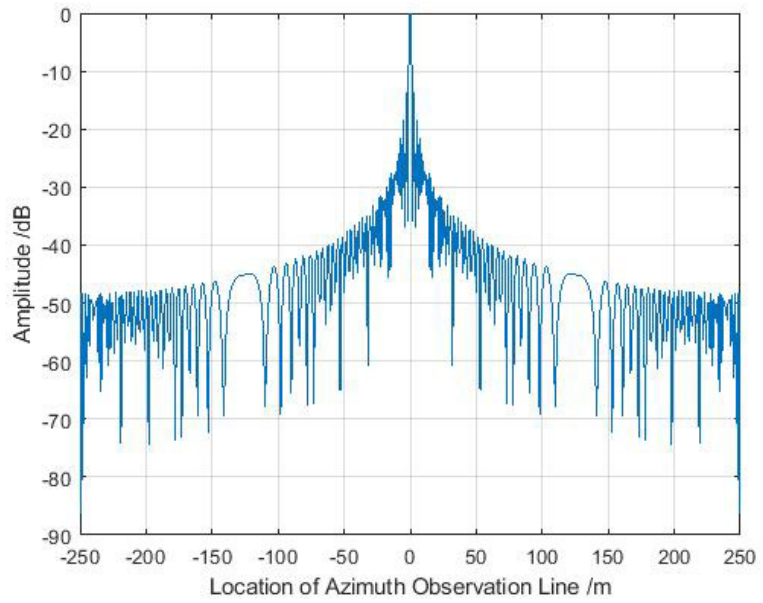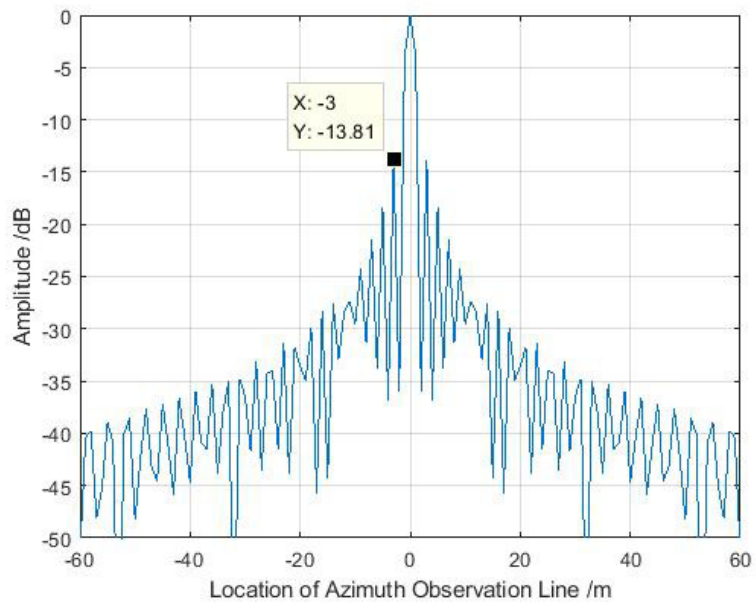Figure 4.6: Conventional beamforming with Blackman window.

(a) Impulse response (point target result) of conventional beamforming with Kaiser window.

(b) Details of mainlobe and sidelobes.

Figure 4.7: Conventional beamforming with Kaiser window(β=2.5).

76

By using the conventional beamforming method to process SAR raw data, we have shown that the beamforming technique in array signal processing can be utilized in SAR data processing to improve the quality of SAR images.

4.2 Least Squares Beamforming Method

4.2.1 Least Squares Beamforming Based SAR Processing Method

The least squares (LS) approach has a long history and has been researched very well in the array signal processing. The aim of beamforming based on least squares approach is to minimize the difference between the designed beam response of this approach and a desired response. In the LS approach, we need to create a desired response, which has the information of the direction angle of main beam, the region of mainlobe and the region of sidelobes. In order to minimize the difference, it is achieved by minimizing a cost function J_{LS} so that we can get the optimal coefficients of weight matrix [32].

As we known, the LS approach is widely used in the array signal processing.We can utilize this approach into the SAR processing by changing the variables of the LS equations. For example, the beam response in the model of array signal processing is based on direction (degrees). In the model of SAR, the beam response is based on the

location of the observation area. Hence, we can change the variable of direction to the variable of location so that we can utilize this method in the SAR processing.

Firstly, we need to analyze the LS problem in the model of array signal processing. Assume the desired beam response is $P_d(\theta)$ and the designed beam response is $P(\theta)$. The desired beam response is the beam response in extremely ideal situation. Usually, we desire the beam response in the mainlobe is 1 and the response in the sidelobe region is 0. However, it is impossible in practical implementation. The response function always attenuates gradually. The designed beam response is the response we receive after designing. We can control by changing the variables of the mainlobe region Θ_m, the sidelobe region Θ_s and the coefficient of sidelobe region α_{LS}. It can be expressed as

$$\boldsymbol{P_d}(\theta) = \boldsymbol{w^H}\boldsymbol{d}(\theta) \tag{4.13}$$

where the $\boldsymbol{w}$ is the weight vector of array, $\boldsymbol{H}$ is the Hermite transpose of matrix and the $\boldsymbol{d}(\theta)$ is the steering vector. The LS based design is formulated by minimizing the squares of error between desired beam response and design beam response over the interested angle Θ, which can be expressed as

$$\min_{w} \int_{\Theta} |P(\theta) - P_d(\theta)|^2 d\theta \tag{4.14}$$

When we does not define the coefficient of sidelobe region, the coefficients of both mainlobe and sidelobe regions are same, which is the unit 1. This means that the coefficient weighting function is not ex-

pressed in the Equation (4.14). However, the coefficients of mainlobe and sidelobe regions are usually different [32] [56]. This means that we need to define the weighting function $v(\theta)$ for this coefficient of the sidelobe region. The weighting function $v(\theta)$ is added to Equation (4.14) and the equation can be re-expressed as

$$\min_{w} \int_{\Theta} v(\theta)|P(\theta) - P_d(\theta)|^2 d\theta \qquad (4.15)$$

For the LS problem, in order to minimize the squares error between the desired beam response and the designed beam response, we need to design a cost function J_{LS}. When the cost function is in the minimum point, we can get the best performance of the designed beam response so that we can have an optimum weight vector. The cost function J_{LS} can be expressed as

$$
\begin{aligned}
J_{LS}(\boldsymbol{w}) &= \int_{\Theta} v(\theta)|P(\theta) - P_d(\theta)|^2 d\theta \\
&= \int_{\Theta} v(\theta)(P(\theta) - P_d(\theta))(P(\theta) - P_d(\theta))^H d(\theta) \\
&= \int_{\Theta} v(\theta)(|P(\theta)|^2 + |P_d(\theta)|^2 - 2Re\{P(\theta)P_d^*(\theta)\}d\theta \\
&= \boldsymbol{w}^H \boldsymbol{G}_{LS}\boldsymbol{w} - \boldsymbol{w}^H \boldsymbol{g}_{LS} - \boldsymbol{g}_{LS}^H \boldsymbol{w} + g_{LS}
\end{aligned}
\qquad (4.16)
$$

where

$$
\begin{aligned}
\boldsymbol{G}_{LS} &= \int_{\Theta} v(\theta)(\boldsymbol{d}(\theta)\boldsymbol{d}^H(\theta))d\theta \\
&= \int_{\Theta} v(\theta)\boldsymbol{D}(\theta)d\theta
\end{aligned}
\qquad (4.17)
$$

$$\boldsymbol{g}_{LS} = \int_{\Theta} v(\theta)(\boldsymbol{d}(\theta)P_d^*(\theta))d\theta \qquad (4.18)$$

$$g_{LS} = \int_{\Theta} v(\theta)|P_d(\theta)|^2 d\theta \qquad (4.19)$$

79

For the solution of the optimum weight vector, we need to take the gradient of the cost function J_{LS} with respect to the weight vector $\boldsymbol{w}$. Setting the cost function to zero so that we can get the optimum weight coefficients of weight vector $\boldsymbol{w}_{opt}$

$$\boldsymbol{w}_{opt} = \boldsymbol{G}_{LS}^{-1}\,\boldsymbol{g}_{LS} \qquad (4.20)$$

The expressions of cost function are all represented by integration operations. However, due to the integration, it is hard to obtain a closed-form solution to the cost function [55] [25]. Instead of the integration of continuous form, we can approximate the cost function with discrete summations giving the discrete form

$$J_{LS_D} = \boldsymbol{w}^H \boldsymbol{G}_D \boldsymbol{w} - \boldsymbol{w}^H \boldsymbol{g}_D - \boldsymbol{g}_D^H \boldsymbol{w} + g_D \qquad (4.21)$$

where

$$\boldsymbol{G}_D = \sum_{\theta_k \in \Theta_m} \boldsymbol{D}(\theta_k) + \alpha_{LS} \sum_{\theta_k \in \Theta_s} \boldsymbol{D}(\theta_k) \qquad (4.22)$$

$$\boldsymbol{g}_D = \sum_{\theta_k \in \Theta_m} \boldsymbol{d}(\theta_k) \qquad (4.23)$$

$$g_D = \sum_{\theta_k \in \Theta_m} 1 \qquad (4.24)$$

θ_k is the direction angles that are of interest. Θ_m is the mainlobe region and Θ_s is the sidelobe region. α_{LS} is the coefficient of sidelobe region.

By using the LS concept, a beamformer based on a 10-element array with adjacent distance of sensors 0.5λ can be designed. The attenuation coefficient of sidelobe α_{LS} is 0.8. The mainlobe region is

set to a single direction of $\Theta_m = 0°$ and the sidelobe region is set to be $\Theta_s \in [-90°, -10°] \cup [10°, 90°]$. The direction angles are sampled every 1°. The response of the designed LS beamformer is shown in Figure 4.8.
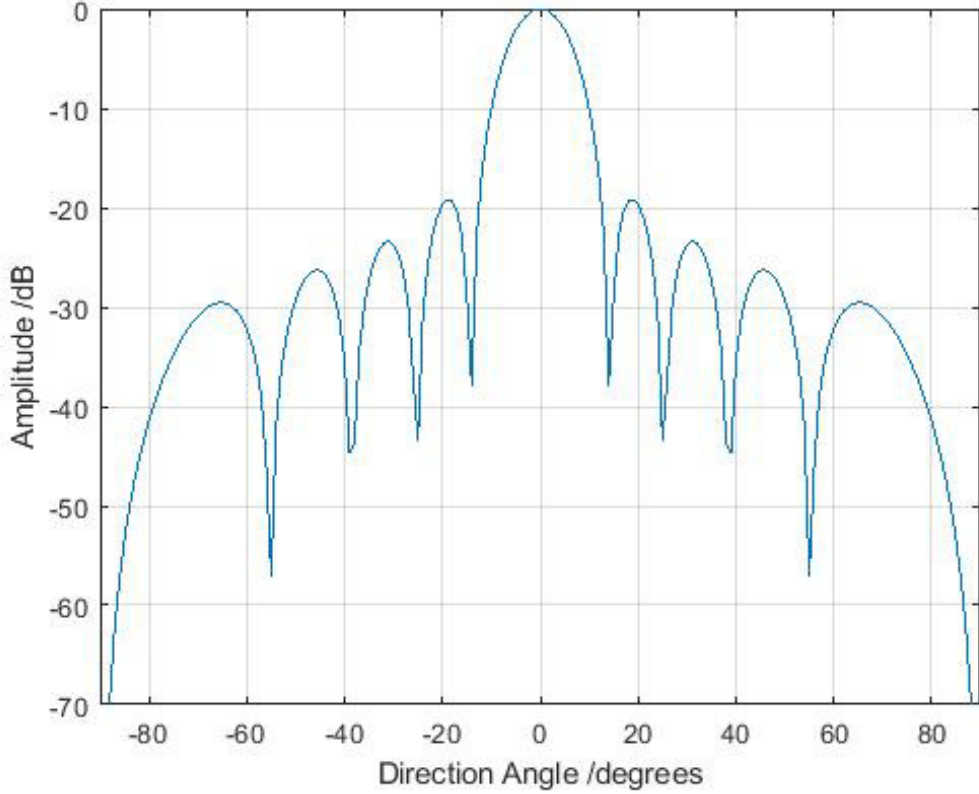
Figure 4.8: Beam response of beamformer based on the least squares.

As shown in Figure 4.8, the mainlobe is at the desired locations of 0°. Also, the value of sidelobe is much attenuated. Compared with conventional beamforming, the value of first sidelobe decreases to -19.16dB, which is much smaller. The width of mainlobe is also in an acceptable value. This means that the LS based beamforming can be utilized in SAR data processing to improve the quality of SAR image [25].

The LS based beamformer designed above is interested in direction angles from $-90°$ to $90°$. However, in the model of SAR, we do not have variable of direction angles. Instead of these angles, we change the direction of interest into the location of interest, which is from X_{min} to X_{max} in the azimuth observation line. This means that the mainlobe region X_m and sideloe region X_s are both described by the location of interest. In SAR processing, we also desire the impulse response (point target result) has a peak value in the location of the point target and other locations are all zero (no sidelobes).The impulse response function in SAR is the same as the beam response in the array signal processing. The function must attenuate gradually. This means that the sidelobes cannot be removed completely. However, we can use variables of the mainlobe region X_m, the sideloe region X_s and the sidelobe coefficient α_{LS} to control and reduce the value of sidelobes. Hence, we can utilize the expressions of LS method in the SAR processing and re-express them to fit the problem in the SAR society. The cost function J_{sar} of SAR processing can be re-expressed as

$$J_{sar} = \boldsymbol{w}^H \boldsymbol{G}_{sar} \boldsymbol{w} - \boldsymbol{w}^H \boldsymbol{g}_{sar} - \boldsymbol{g}_{sar}^H \boldsymbol{w} + g_{sar} \qquad (4.25)$$

where

$$\boldsymbol{G}_{sar} = \sum_{x_k \in X_m} \boldsymbol{D}(x_k) + \alpha_{LS} \sum_{x_k \in X_s} \boldsymbol{D}x_k) \qquad (4.26)$$

$$\boldsymbol{g}_{sar} = \sum_{x_k \in X_m} \boldsymbol{d}(x_k) \qquad (4.27)$$

$$g_{sar} = \sum_{x_k \in X_m} 1 \tag{4.28}$$

The optimal weight vector is also represented as

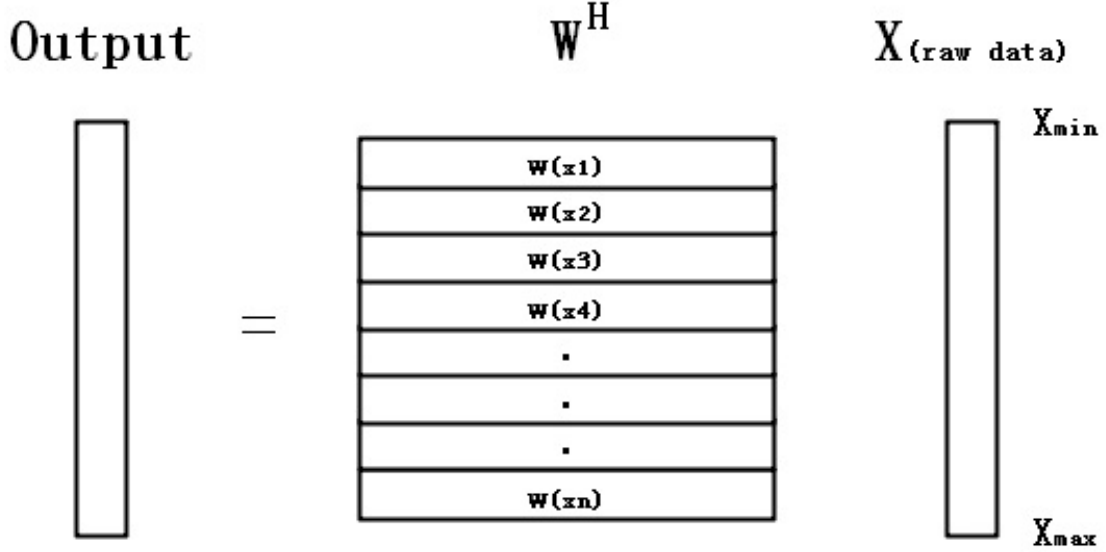$$\boldsymbol{w}_{opt_{sar}} = \boldsymbol{G}_{sar}^{-1} \, \boldsymbol{g}_{sar} \tag{4.29}$$

Figure 4.9: Steps of SAR processing based on the least squares beamforming.

This optimal weight vector for SAR is to make the beam point to a location in the azimuth observation line, such as 0m, -10m and 10m. In order to cover the whole observation line, we are going to build many sets of weight vectors pointing to different locations. Figure 4.9 shows the steps of SAR processing based on LS, where X is the SAR raw data vector, which has a size of $M \times 1$. W is the weighting vector matrix pointing to different locations. The beam of $w(x_1)$ is pointing to the location of X_{min} and $w(x_n)$ is pointing to X_{max}. In the observation area from X_{min} to X_{max}, the locations are discretized into n points to create n beams pointing to different locations to create the

SAR image.

In the LS based SAR processing method, we can select different values of mainlobe region X_m, sidelobe region X_s and attenuation coefficient α_{LS} to make a balance between mainlobe width and sidelobe value. The aim of this method is to find a better balance to improve the quality of SAR image.

4.2.2   Simulation Results

In this section, some simulation results of the least squares beamforming methods are provided. The basic parameters to build the SAR model is the same as the simulations in section 3.1. The azimuth observation area is still from $X_{min} = -500m$ to $X_{max} = 500m$. The distance between two adjacent sampling points is still $d = 1m$ and the number of sampling points is $M = 1001$. This means that the size of the raw data vector is $M \times 1 = 1001 \times 1$. The distance between two beams pointing to two adjacent locations is set to 1m. The beams created by weight vector matrix are pointed to -500m,-499m,...500m. This is to make the weight vector matrix into a square matrix. This means that the size of the output vector is the same as the size of raw data vector. The attenuation coefficient α_{LS} is set to 0.8 and always keep fixed.

We can change the mainlobe region and sidelobe region to obtain

different results. For the weight vector pointing to location $x = 0m$, the mainlobe region is designed to be the single point $X_m = 0m$ and the sidelobe region is designed to $X_s \in [-500, -\Delta_s] \cup [\Delta_s, 500]$ being sampled every 1m. We are going to create beams pointing to different locations. The general descriptions of mainlobe region and sidelobe region are $X_m = x(k)$ and $X_s \in [-500, -\Delta_s + x(k)] \cup [\Delta_s + x(k), 500]$, respectively. Δ_s is a variable to change the sidelobe region selection. In the following simulations, we choose Δ_s=50m, 80m and 120m.

Figures 4.10, 4.11 and 4.12 show the simulation results of SAR processing method based on the least squares beamforming with different sidelobe regions. Compared with simulation results of conventional beamforming (matched filter) with windows, it is clear that the value of sidelobe has decreased. This means that the sidelobe effect has been reduced using this least squares beamforming based method. The width of mainlobe keeps the same with conventional beamforming (matched filter). By comparing the value of sidelobe and the width of mainlobe, the method based on the least squares beamforming improves the quality of SAR image by reducing the levels of sidelobe.
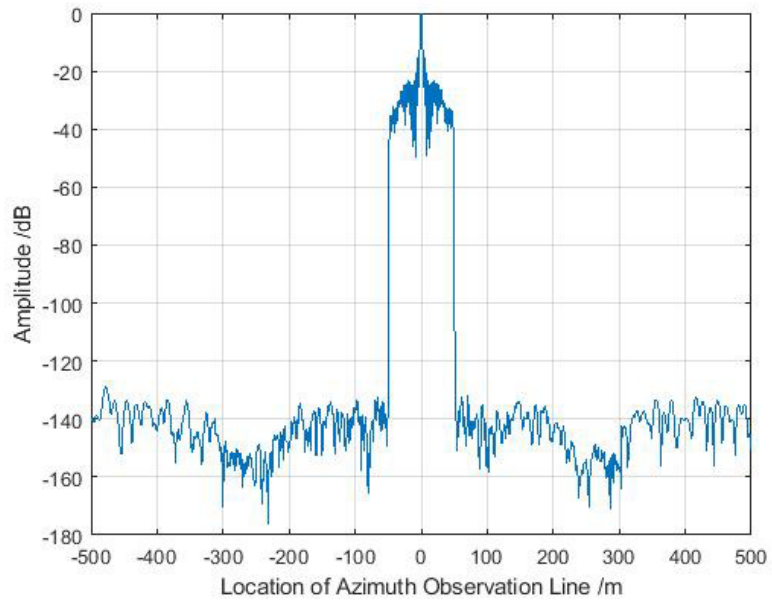
(a) Impulse response (point target result) of SAR processing method based on the least squares beamforming for Δ_s=50m.
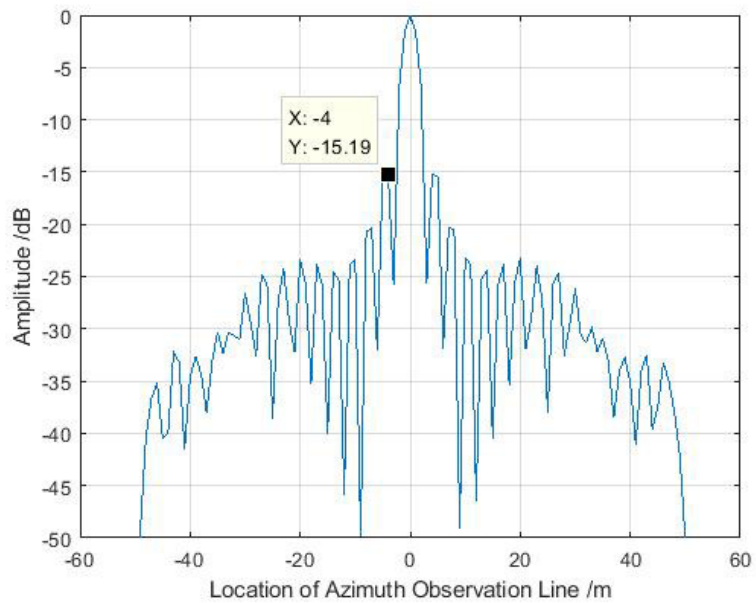
(b) Details of mainlobe and sidelobes.

Figure 4.10: SAR processing method based on the least squares beamforming for Δ_s=50m.

86

(a) Impulse response of SAR processing method based on the least squares beamforming for Δ_s=80m.

(b) Details of mainlobe and sidelobes.

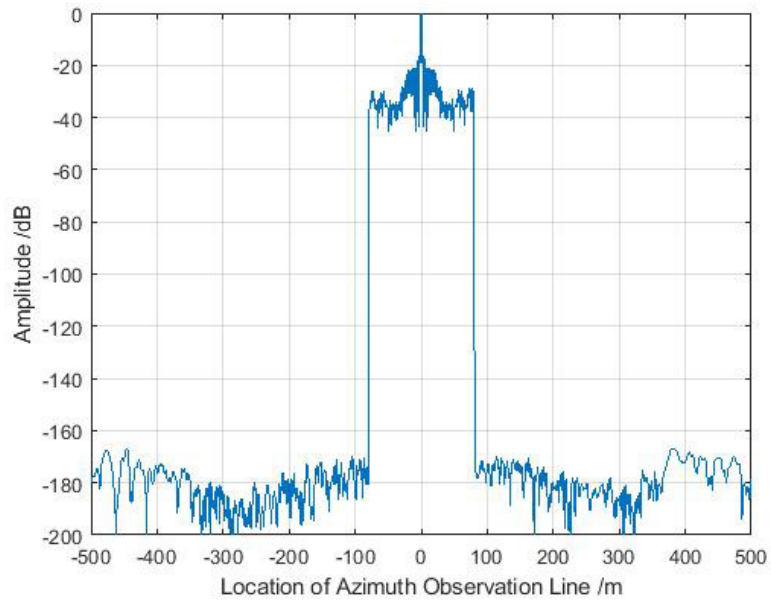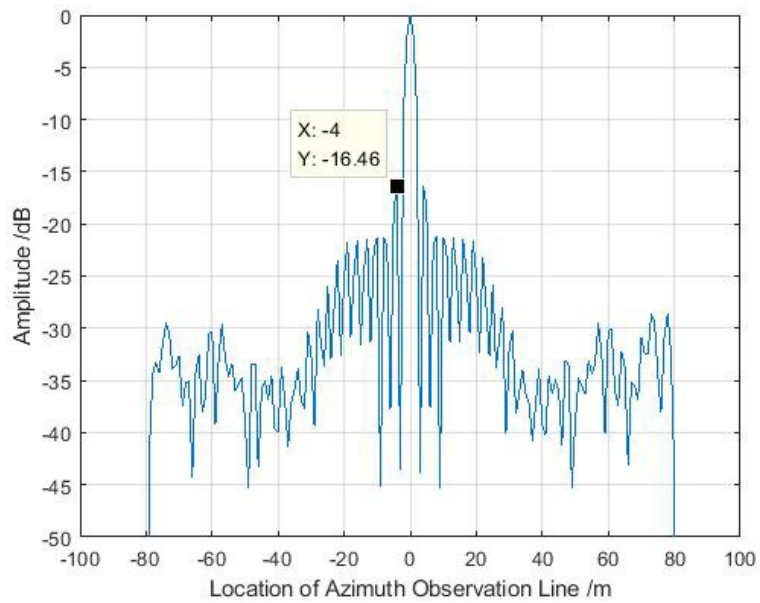Figure 4.11: SAR processing method based on the least squares beamforming for Δ_s=80m.

(a) Impulse response (point target result) of SAR processing method based on the least squares beamforming for Δ_s=120m.
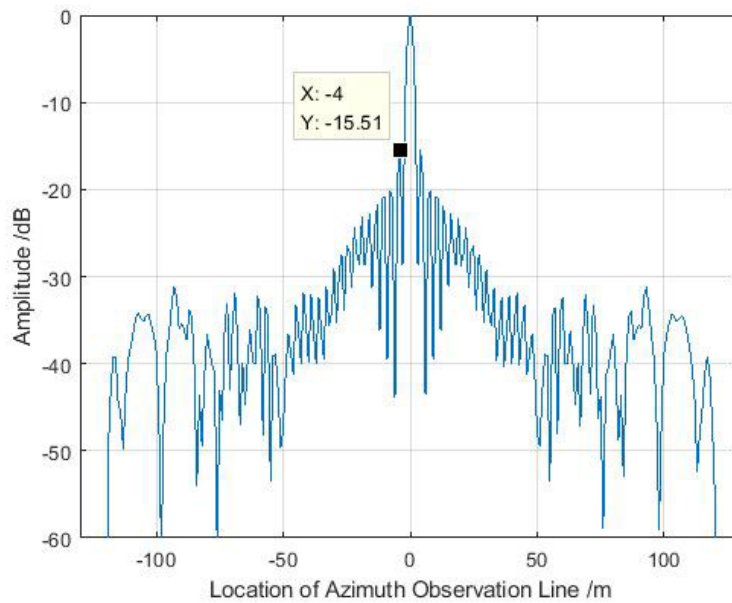
(b) Details of mainlobe and sidelobes.

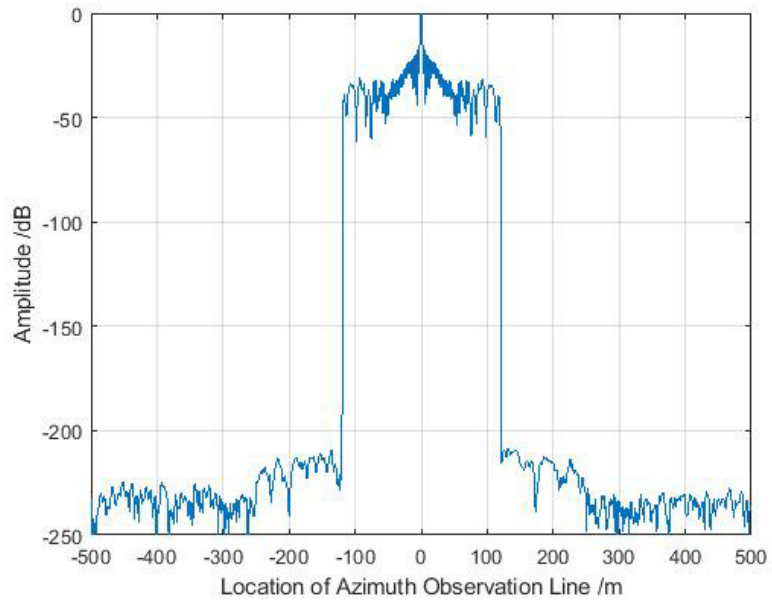Figure 4.12: SAR processing method based on the least squares beamforming for Δ_s=120m.

Chapter 5

Conclusions and Future Work

5.1 Conclusions

In this thesis, the range-Doppler algorithm and CopSAR concept are introduced. Also, the least squares beamforming based processing method is utilized in the processing of SAR raw data. The simulation results of this method show that the processing method based on beamforming can mitigate the value of side lobes and improve the quality of SAR image. The processing methods of array signal processing can be used in the society of SAR for a higher resolution. The beamforming method based on sparse arrays and compressed sensing can be researched to utilize in the SAR data processing in the future work.

5.2 Future Work

In this thesis, a method based on the least squares beamforming is utilized in the processing of SAR data. There are some other array signal processing techniques which can be utilized in SAR data processing, such as beamforming method based on sparse array for SAR data processing and beamforming method under the framework of compressed sensing for SAR data processing. So for the future work, three potential research aspects are introduced in the following parts.

5.2.1 Beamforming Method Based on Sparse Arrays

Firstly, we can apply the concept of sparse array beamforming in SAR. In the section 3.2, the CopSAR based on co-prime array has considered to utilize sparse arrays into SAR model and data processing. However, it only uses the concept of sparse arrays. The processing method is still based on the matched filter. This means that this CopSAR still has many limitations and disadvantages, which have been analyzed in the subsection 3.2.2. Hence, we must use the beamforming method based on sparse arrays to solve these problems. By trying different types of sparse arrays, such as nested array [38], co-prime array [54] [51] and extended co-prime array [40], we are going to compare them and choose one kind of sparse array which can achieve the best imaging quality. There is an important problem to solve. In conventional SAR, the virtual array pattern is always ULA for different point targets in

the observing area. However, for a sparse array, the array pattern will be different for different point targets. This problem must be considered and solved if we want to utilize sparse array in the beamforming based processing approach. When this problem is solved, SAR will not transmit and receive pulses with a constant PRF any more. Instead of virtual ULA, SAR can transmit and receive pulses in terms of a sparse array. This will reduce the amount of data significantly.

5.2.2 Beamforming Method Under the Framework of Compressed Sensing

Then, we can use the concept of compressed sensing and combine it with the beamforming method. In [48], the proposed DoA estimation approach is under the framework of compressed sensing. By using the sparsity property of signals, reconstruction algorithm (l_1 norm minimization) based on compressed sensing can estimate the direction of impinging signals by using fewer amount of data than conventional DoA estimation algorithms. If we utilize this method in SAR, the amount of data will decrease further and the effect of sidelobes will be mitigated using the reconstruction algorithms. However, the SAR data is sparse when it only has several point targets or small area target. The data does not have sparsity property when it has large area target (many reflected targets on the entire observing areas). In this scenario, we need to research for solutions to use compressed sensing. Firstly, in the observing area, the back-scattered reflection coefficient

could be low and the echo of these targets can be seen as noise. Then, the SAR echo data can be seen as sparse signal and can utilize compressed sensing to process it. If the targets are all with high reflected coefficients, the raw data cannot be seen as sparse signal.

Bibliography

[1] Range-doppler algorithm analysis. Accessed 30-November-2018. https://www.dropbox.com/s/75347bh9f1860ja/Range-Doppler_Algorithm_Analysis.doc?dl=0.

[2] Thomas P Ager. An introduction to synthetic aperture radar imaging. *Oceanography*, 26(2):20–33, 2013.

[3] Richard Bamler. A comparison of range-doppler and wavenumber domain sar focusing algorithms. *IEEE Transactions on Geoscience and Remote Sensing*, 30(4):706–713, 1992.

[4] Richard G Baraniuk. Compressive sensing [lecture notes]. *IEEE signal processing magazine*, 24(4):118–121, 2007.

[5] John R Bennett and Ian G Cumming. A digital processor for the production of seasat synthetic aperture radar imagery. In *LARS Symposia*, page 316, 1979.

[6] Sujit Bhattacharya, Thomas Blumensath, Bernard Mulgrew, and Mike Davies. Fast encoding of synthetic aperture radar raw data using compressed sensing. In *Statistical Signal Processing, 2007. SSP'07. IEEE/SP 14th Workshop on*, pages 448–452. IEEE, 2007.

[7] Han Bing and Wang Pengbo. The research of sar imaging based on co-prime arrays sampling. *Advances in Engineering Research*, pages 272–277, 2017.

[8] Ciro Cafforio, Claudio Prati, and Fabio Rocca. Sar data focusing using seismic migration techniques. *IEEE transactions on aerospace and electronic systems*, 27(2):194–207, 1991.

[9] Emmanuel J Candes and Terence Tao. Decoding by linear programming. *IEEE transactions on information theory*, 51(12):4203–4215, 2005.

[10] Emmanuel J Candès and Michael B Wakin. An introduction to compressive sampling. *IEEE signal processing magazine*, 25(2):21–30, 2008.

[11] Yee Kit Chan and Voon Chet Koo. An introduction to synthetic aperture radar (sar). *Progress In Electromagnetics Research*, 2:27–60, 2008.

[12] I.G. Cumming and F.H. Wong. *Digital Processing of Synthetic Aperture Radar Data: Algorithms and Implementation*. Artech House, 2005.

[13] John C Curlander and Robert N McDonough. *Synthetic aperture radar*, volume 396. John Wiley & Sons New York, NY, USA, 1991.

[14] LJ Cutrona. Synthetic aperture radar. *Radar handbook*, 2:2333–2346, 1990.

[15] GW Davidson, Ian G Cumming, and MR Ito. A chirp scaling approach for processing squint mode sar data. *IEEE Transactions on Aerospace and Electronic Systems*, 32(1):121–133, 1996.

[16] Gerardo Di Martino and Antonio Iodice. Coprime synthetic aperture radar (copsar): A new acquisition mode for maritime surveillance. *IEEE Transactions on Geoscience and Remote Sensing*, 53(6):3110–3123, 2015.

[17] Gerardo Di Martino and Antonio Iodice. Orthogonal coprime synthetic aperture radar. *IEEE Transactions on Geoscience and Remote Sensing*, 55(1):432–440, 2017.

[18] Gerardo Di Martino, Antonio Iodice, and Stefano Medagli. Orthogonal coprime sar. In *Geoscience and Remote Sensing Symposium (IGARSS), 2015 IEEE International*, pages 3758–3761. IEEE, 2015.

[19] David L Donoho. Compressed sensing. *IEEE Transactions on information theory*, 52(4):1289–1306, 2006.

[20] David L Donoho. For most large underdetermined systems of linear equations the minimal l1-norm solution is also the sparsest solution. *Communications on Pure and Applied Mathematics: A Journal Issued by the Courant Institute of Mathematical Sciences*, 59(6):797–829, 2006.

[21] Jian Fang, Zongben Xu, Bingchen Zhang, Wen Hong, and Yirong Wu. Fast compressed sensing sar imaging based on approximated

observation. *IEEE Journal of Selected Topics in Applied Earth Observations and Remote Sensing*, 7(1):352–363, 2014.

[22] Albert C Fannjiang, Thomas Strohmer, and Pengchong Yan. Compressed remote sensing of sparse objects. *SIAM Journal on Imaging Sciences*, 3(3):595–618, 2010.

[23] Lal Chand Godara. Application of antenna arrays to mobile communications. ii. beam-forming and direction-of-arrival considerations. *Proceedings of the IEEE*, 85(8):1195–1245, 1997.

[24] Grant Hampson et al. Simulation of beamforming techniques for the linear array of transducers. 1995.

[25] Matthew Blair Hawes. *Efficient Design of Sparse Arrays for Narrowband and Wideband Beamforming*. PhD thesis, University of Sheffield, 2014.

[26] W Hughes, K Gault, and GJ Princz. A comparison of the range-doppler and chirp scaling algorithms with reference to radarsat. In *Geoscience and Remote Sensing Symposium, 1996. IGARSS'96.'Remote Sensing for a Sustainable Future.', International*, volume 2, pages 1221–1223. IEEE, 1996.

[27] Christopher R Jackson, John R Apel, et al. *Synthetic aperture radar: marine user's manual*. US Department of Commerce, National Oceanic and Atmospheric Administration, National Environmental Satellite, Data, and Information Serve, Office of Research and Applications, 2004.

[28] RMcDonough JCurlander. Synthetic aperture radar: Systems and signal processing, 1991.

[29] Michael Y Jin and Chialin Wu. A sar correlation algorithm which accommodates large-range migration. *IEEE Transactions on Geoscience and Remote Sensing*, (6):592–597, 1984.

[30] Gerhard Krieger, Marwan Younis, Sigurd Huber, Federica Bordoni, Anton Patyuchenko, Junghyo Kim, Piotr Laskowski, M Villano, T Rommel, P Lopez-Dekker, et al. Digital beamforming and mimo sar: Review and new concepts. In *Synthetic Aperture Radar, 2012. EUSAR. 9th European Conference on*, pages 11–14. VDE, 2012.

[31] Tukaram Baburao Lavate, VK Kokate, and AM Sapkal. Performance analysis of music and esprit doa estimation algorithms for adaptive array smart antenna in mobile communication. In *Second International Conference on Computer and Network Technology*, pages 308–311. IEEE, 2010.

[32] Wei Liu and Stephan Weiss. *Wideband beamforming: concepts and techniques*, volume 17. John Wiley & Sons, 2010.

[33] Di Martino and Antonio Iodice. Coprime synthetic aperture radars. In *Research and Technologies for Society and Industry (RTSI), 2017 IEEE 3rd International Forum on*, pages 1–4. IEEE, 2017.

[34] Josef Mittermayer, Alberto Moreira, and Otmar Loffeld. Spotlight sar data processing using the frequency scaling algorithm. *IEEE Transactions on Geoscience and Remote Sensing*, 37(5):2198–2214, 1999.

[35] Alberto Moreira, Josef Mittermayer, and Rolf Scheiber. Extended chirp scaling algorithm for air-and spaceborne sar data processing in stripmap and scansar imaging modes. *IEEE Transactions on Geoscience and Remote Sensing*, 34(5):1123–1136, 1996.

[36] David C Munson, James Dennis O'brien, and W Kenneth Jenkins. A tomographic formulation of spotlight-mode synthetic aperture radar. *Proceedings of the IEEE*, 71(8):917–925, 1983.

[37] H Ohkura, T Jitsufuchi, T Matsumoto, and Y Fujinawa. Application of sar data to monitoring of earthquake disaster. *Advances in Space Research*, 19(9):1429–1436, 1997.

[38] Piya Pal and PP Vaidyanathan. Nested arrays: A novel approach to array processing with enhanced degrees of freedom. *IEEE Transactions on Signal Processing*, 58(8):4167–4181, 2010.

[39] Shruti Parwana and Sanjay Kumar. Analysis of lfm and nlfm radar waveforms and their performance analysis. *International Research Journal of Engineering and Technology*, 2(2), 2015.

[40] Shen Qing, Liu Wei, Cui Wei, and Wu Siliang. Extension of coprime arrays based on the fourth-order difference co-array concept. *IEEE Signal Processing Letters*, 23(5):615–619, 2016.

[41] Jessica R. Exploring venus with sar. *Venus Seminar*, 2015.

[42] Shivakumar Ramakrishnan, Vincent Demarcus, Jerome Le Ny, Neal Patwari, and Joel Gussy. Synthetic aperture radar imaging using spectral estimation techniques. *Advanced Signal Processing*, 2002.

[43] HO Ramp and ER Wingrove. Principles of pulse compression. *IRE Transactions on Military Electronics*, 1051(2):109–116, 1961.

[44] R Keith Raney, Hartmut Runge, Richard Bamler, Ian G Cumming, and Frank H Wong. Precision sar processing using chirp scaling. *IEEE Transactions on geoscience and remote sensing*, 32(4):786–799, 1994.

[45] A Reigber, A Potsis, E Alivizatos, N Uzunoglu, and A Moreira. Wavenumber domain sar focusing with integrated motion compensation. In *INTERNATIONAL GEOSCIENCE AND REMOTE SENSING SYMPOSIUM*, volume 3, pages III–1465, 2003.

[46] Andreas Reigber, E Alivizatos, A Potsis, and Alberto Moreira. Extended wavenumber-domain synthetic aperture radar focusing with integrated motion compensation. *IEE Proceedings-Radar, Sonar and Navigation*, 153(3):301–310, 2006.

[47] Matthew Schlutz. Synthetic aperture radar imaging simulated in matlab. 2009.

[48] Qing Shen, Wei Liu, Wei Cui, and Siliang Wu. Underdetermined doa estimation under the compressive sensing framework: A review. *IEEE Access*, 4:8865–8878, 2016.

[49] Mg Siegler. Geoeye-1, the "google satellite," will capture the obama inauguration from space. Accessed 02-December-2018. https://venturebeat.com/2009/01/16/geoeye-1-the-google-satellite-will-capture-the-inauguration-from-space/.

[50] Mehrdad Soumekh. *Synthetic aperture radar signal processing*, volume 7. New York: Wiley, 1999.

[51] Palghat P Vaidyanathan and Piya Pal. Sparse sensing with co-prime samplers and arrays. *IEEE Transactions on Signal Processing*, 59(2):573–586, 2011.

[52] Barry D Van Veen and Kevin M Buckley. Beamforming: A versatile approach to spatial filtering. *IEEE assp magazine*, 5(2):4–24, 1988.

[53] Kush R Varshney, Müjdat Çetin, John W Fisher, and Alan S Willsky. Sparse representation in structured dictionaries with application to synthetic aperture radar. *IEEE Transactions on Signal Processing*, 56(8):3548–3561, 2008.

[54] Xiaomeng Wang, Xin Wang, and Xuehong Lin. Co-prime array processing with sum and difference co-array. In *Signals, Systems and Computers, 2015 49th Asilomar Conference on*, pages 380–384. IEEE, 2015.

[55] Yong Zhao, Wei Liu, and Richard Langley. A least squares approach to the design of frequency invariant beamformers. In *Signal Processing Conference, 2009 17th European*, pages 844–848. IEEE, 2009.

[56] Yong Zhao, Wei Liu, and Richard J Langley. Subband design of fixed wideband beamformers based on the least squares approach. *Signal Processing*, 91(4):1060–1065, 2011.